Phoenix (PHX) Project

MET LIDAR

Characterization & Calibration Report

Version 1.0

Prepared by:
James Whiteway, Leonce Komguem, and Cameron Dickinson

MET Document Manager:
Cameron Dickinson

Prepared by: **Cameron Dickinson** Phoenix MET Team	
Approved by: **Jim Whiteway** Instrument Co-Investigator, MET	**Leslie Tamppari** Phoenix Project Scientist
Dr. Reta Beebe Director, PDS Atmospheres Node	**Ed Grayzeck** Project Manager, Planetary Data System

Revision and History Page

Rev.	Description	Date
1.0	Document Start	03/03/08

TBD Items

Section	Description

1 PURPOSE AND SCOPE OF DOCUMENT

This document provides users of the Phoenix MET (Meteorological) data producst with a detailed description of the characterization activities relating to the atmospheric Lidar instrument

It is intended to provide enough information to enable users to read and understand background information relating to the data products. The users for whom this document is intended are the scientists who will analyze the data, including those associated with the project and those in the general planetary science community.

This report describes the characterization of the lidar instrument on the Phoenix mission to Mars. The work was carried out in the laboratory and in field campaigns. The laboratory activity involved atmospheric measurements with the flight model of the Phoenix lidar while it was operating within a thermal vacuum chamber with pressure, temperature and composition similar to what will be encountered on Mars. These measurements characterize the fidelity of the lidar system in recording signals that provide an accurate representation of the atmosphere. The laboratory measurements have provided a calibration for the optical throughput of the lidar system, characterized the nonlinear response of the signal acquisition electronics, and determined the variation in the transmitter-receiver alignment over the range of temperatures expected during the mission. It was also demonstrated that the requirements on the performance characteristics of the lidar have been satisfied.

2 APPLICABLE DOCUMENTS

[1] MET Lidar SIS Document

[2] MET Lidar EDR/RDR Archive Volume SIS Document

3 INTRODUCTION

Field measurement campaigns were conducted with a lidar system that has similar characteristics to the Phoenix lidar. The goal was to develop methods for determining atmospheric properties from the lidar measurements, and to provide a basis for the scientific interpretation. The field campaigns have involved combining the lidar remote sensing with aircraft in situ measurements. Two aspects of the Martian atmosphere that the lidar will observe are ice clouds and airborne desert dust. Ice clouds at temperature and humidity similar to Mars can be found in the Earths atmosphere at the tropopause: cirrus clouds in the height range 10 to 18 km. Combined lidar and aircraft in situ ice crystal measurements have been used to develop a method to derive the cloud ice water content from the lidar measurements. Field measurement campaigns concentrating on airborne desert dust have been carried out in the deserts of Arizona and Australia. The Australian campaign was carried out in November 2007, so the results concerning desert dust will be included in the final version of this report (March 2008).

4 SCIENCE BACKGROUND

The Phoenix mission to Mars [Smith et al. 2008] will advance our knowledge of the climate on Mars by combining lidar remote sensing of atmospheric dust and clouds [Whiteway et al. 2008] with measurements of solar radiation [Lemmon et al. 2008] and in situ sampling of temperature, pressure, wind [Taylor et al. 2008], and water vapour [Zent et al. 2008].

Day to day variation of the local weather on Mars is controlled primarily by the amount of solar radiation reaching the surface and this depends on the optical thickness of the dust suspended in the atmosphere. This affects local and global meteorological patterns which in turn determine the lifting of dust from the surface and long range transport [Leovy 2001; Newman et al. 2002]. There is also a climate interaction with the distribution of water ice above and below the surface of Mars [Boynton et al. 2002, Pathak et al. 2008]. This involves transport of water through the atmosphere, and previous lidar measurements from orbit have indicated that clouds play a substantial role [Neumann et al. 2003].

The lidar on the Phoenix mission will record the height profile of laser backscatter from the dust and cloud layers that drift past the landing site with a view that is continuous in time. The attenuation of the lidar signal can be used to derive the optical extinction coefficient and this is related to atmospheric properties. For example, the extinction of solar radiation due to dust has a first order effect on heating of the surface of Mars. The measured optical extinction can also be related to the amount of scattering material. For example, for a thin cloud the extinction coefficient measured by a lidar can be used to derive the ice water content within the cloud [Heymsfield et al. 2005]. Such a measurement will be of vital importance to the mission goal to investigate water on Mars. The combination of the lidar and passive remote sensing with in situ sampling will provide a view of the interacting processes that determine the local weather at the surface and also the role of the atmosphere in the water cycle on Mars.

5 LIDAR INSTRUMENT

A basic atmospheric lidar (light detection and ranging) emits pulses of laser light into the atmosphere, and it detects and records the backscattered light as a function of time (Measures, 1984). The time resolved signal is converted to distance using the speed of light and a factor of two to account for the round-trip path length. The Phoenix lidar operates in this manner with the characteristics listed in Table 1. A schematic diagram is shown in Fig. 1 and a photograph of the system with the cover removed is shown in Figure 2.

A drawing of the lidar transmitter assembly is shown in Fig. 3. It is based on a diode pumped, passively Q-switched, neodymium-doped yttrium aluminium garnet (Nd:YAG) laser. This configuration was chosen for its robustness and technological maturity as much as for its suitable lidar performance. The pump diode array emits at a wavelength of 808 nm and is used to provide the energy to the Nd:YAG crystal within the laser cavity. Lasing is inhibited within the cavity through the use of a saturable absorber. The photon density within the oscillator cavity builds to a level where the saturable absorber bleaches and the energy within the cavity is dumped as a laser pulse over a very short time (a passive Q-switch). For this laser the output light pulse has a length of 10 ns and an energy of 0.7 mJ.

After the laser cavity emits a light pulse, part of the optical energy is converted from a wavelength of 1064 nm to 532 nm by second harmonic generation in a Potassium Titanyl Phosphate (KTP) crystal. The laser output is then expanded by a factor of 10 in order to reduce the divergence to 0.5 mrad. A small fraction of the outgoing laser pulse is "picked off" and separated into the two wavelength components in order to measure the relative amplitude of each wavelength with photodiodes. The signal from the photodiode detecting the 1064 nm pulse is used to trigger the data acquisition electronics, providing a zero-time reference, and also to shut off the pumping diodes.

Figure 1 shows how the backscatter signals are collected by an afocal reflective telescope and split into the two relevant wavelengths using dichroic mirrors. The 1064 nm backscatter is detected by an Avalanche Photo-Diode (APD), and recorded using 14-bit analog to digital conversion (ADC). The 532 nm backscatter is detected by a Photomultiplier (PMT) and the signal is recorded using both ADC and photon counting. Photon counting is required to record the weak signals from heights above 5 km and up to 20 km.

The signal as a function of height is integrated over a set number of laser pulses and height bins. For example the standard operating mode is to use 50m vertical resolution (ten 5-meter bins averaged) and 10 second temporal resolution (1000 laser pulses averaged). These profiles are then stored sequentially. The temporal and spatial averaging are parameters that are part of the commands transmitted from the ground station during the mission.

6 LIDAR TESTING AND VERIFICATION

Verification that the Phoenix lidar will function on Mars was achieved by operating it within a thermal vacuum (T-vac) chamber at the pressures and temperatures expected on the surface of Mars (e.g. 8 Torr, -70° C). A window was installed in the T-vac chamber so that the output laser pulses and the receiver field of view could be directed across the clean room and through another window into the atmosphere in the zenith direction. Atmospheric observations could then be acquired and compared with simultaneous measurements with two other lidar systems. Photographs of these facilities are shown in Figures 4 to 7.

The lidar used for side-by-side comparison in testing and validation was supplied by York University (referred to as the York Lidar). This has the same essential characteristics as the Phoenix Lidar. For example, the transmitted wavelengths are the same (1064 nm and 532 nm), and the same detectors are applied in the receiver. The data acquisition electronics provide the same function as in the Phoenix lidar: analog to digital conversion (ADC) at 1064 nm; both ADC and photon counting at 532 nm. The main difference is that the York Lidar has a more powerful laser than the Phoenix lidar. Photographs of the York Lidar are shown in Figs. 8 and 9.

Another lidar was provided by Dalhousie University. This lidar operated at a wavelength of 532 nm. It had different characteristics from the Phoenix lidar, but the useful feature of this lidar that was that it used a receiver with a field of view of 10 mrad. This was useful for characterizing the overlap between the transmitter and receiver in the Phoenix lidar.

The alignment of the Phoenix lidar in Mars conditions was verified by direct comparison to the York Lidar with simultaneous atmospheric measurements. An example of a comparison between the York lidar and Phoenix lidar with photon counting signal acquisition is shown in Fig. 10. The Phoenix lidar was in the T-vac chamber with 8 Torr of CO_2 at a temperature of -70° C, and the lidar chassis temperature was -36° C. The ratio of the signals from the two lidars is constant with height up to above 15 km and this is an indication that the Phoenix lidar transmitter is aligned within the receiver field of view. Another indication that the system is properly aligned is in the comparison with the expected signal from molecular backscatter.

There is an enhancement in the signal in Fig. 10 between heights of 8.5 km and 10.5 km due to a cirrus cloud layer. There is also a thin cloud at a height of 1.5 km. It is expected that such thin ice clouds will be detected in the atmosphere of Mars.

Below a height of 2 km there is a reduction in the signals recorded with both lidars in comparison with the expected molecular backscatter signal. This is a well known effect: the photon counting saturates due to electrical pulse overlap at count rates greater than 5 MHz. This nonlinear effect in the photon counting has been characterized (Sec. 6) and can be corrected when there is not substantial variability within the averaging period. However, there is no saturation in the signal recorded by analog to digital conversion.

Figure 11 shows the 532 nm signal recorded by amplitude to digital conversion (ADC). The ratio of the Phoenix Lidar to the York Lidar signals is constant with height above about 400m. The difference below 600 m is due to incomplete overlap between the outgoing laser pulse and the receiver FOV. There is complete overlap above 600 m (at this temperature). Correction for the signal reduction in the incomplete overlap region is crucial for accurate measurements at the lowest heights. A temperature dependent correction method has been developed and this is described in Sec. 5.

7 VARIATION OF LIDAR ALIGNMENT WITH TEMPERATURE

The most important part of the testing was to ensure that the receiver and transmitter remain aligned over the full range of temperatures that are expected during the mission. The temperature within the lidar is controlled by heaters and the coldest it will get during the mission is -40° C. The heat dissipated by the laser while operating will increase the temperature of the instrument by about 5° C over a 15 minute interval. The baseline plan is to have the lidar operate for four separate 15 minute intervals at mid-day, evening, midnight and morning. In this scenario the temperature of the lidar chassis in not expected to rise above -20° C. If the lidar is run for longer periods and more often, then the lidar chassis will get warmer. The alignment of the transmitter was optimized so that it was pointing within the receiver telescope FOV over a temperature range of -40° C to -0° C on the lidar chassis.

The direction of the transmitted laser light relative to the receiver telescope field of view (FOV) was determined by deflecting the transmitted light with a variable optical wedge. The direction of the transmitted light was deflected until the atmospheric backscatter signal at a height of 1.5 km started to decrease and this was done in each of the four cardinal directions. The outline of the FOV could then be determined relative to the transmitter output. This was done at various temperatures between -40° C and 0° C. It was determined that the relative angle between the transmitted light pulse and the receiver telescope FOV axis changed by 0.9 mrad over the temperature range from -40ºC to 0ºC, moving inward toward the telescope axis as the temperature increased. The transmitted light pulse has a divergence of 0.5 mrad, so there is 1 mrad of tolerance within the 1.5 mrad FOV to account for temperature variations. Thus it was possible to optimize the alignment of the system so that the transmitter is pointing within the FOV over the range of temperature from -40ºC to 0ºC. This was done so that at -40ºC the transmitter output is pointing 0.4 mrad away from the central axis of the receiver telescope FOV. It is still within the full 1.5 mrad of the FOV, with a 0.1 mrad tolerance between the outside edge of the transmitted laser pulse and the edge of the FOV. At a temperature of 0º C the transmitter was pointing 0.5 mrad toward the receiver telescope. This is summarized in Table 2.

8 VARIATION OF TRANSMITTER-RECIEVER OVERLAP WITH TEMPERATURE

Figures 12 and 13 illustrate the relative angular alignment between the transmitter and receiver. There is a region near the ground where there is incomplete overlap between the transmitted laser output and the conical receiver field of view. For example, at a temperature of -40º C (Figs. 12 and 14) the overlap starts at a height of 125 m and is complete at a height of 1170 m. In between these heights the overlap between the transmitter and receiver is incomplete. The recorded signal will be reduced by a factor that is equal to the fraction of laser beam cross-sectional area that is contained within the receiver field of view.

This reduction in signal was determined by taking the ratio to the of the Phoenix lidar signal to the York and Dalhousie lidars. The York lidar has full overlap above about 100 m, and the Dalhousie lidar has full overlap above about 10 m. The ratio of Phoenix/York has been used above 500m and the ratio Phoenix/ Dalhousie has been used below 500 m. (The signal recorded with the Dalhousie system was too weak to be used above 500m). Figure 14 shows the ratio as a function of height above the ground at temperatures of -40º C and -10º C. This is referred to as the overlap function. The inverse of this is the correction function.

Figure 14 illustrates how the incomplete overlap region changes with temperature. At a temperature of -40º C the top of the incomplete overlap region is at 1170 m, but at a temperature of -10º C the top of the overlap region is at 150 m. The height at which the overlap begins also changes with the temperature. The characteristics of the incomplete overlap region at each temperature used in testing are given in Table 3.

A correction must be applied to the data that compensates for the incomplete overlap. If the alignment did not change with temperature, then this would only require one overlap correction function. During the mission, measurements will be acquired at arbitrary temperatures that are not the same as the temperatures at which the measurements were acquired during testing. It is then required to interpolate the overlap function between different temperatures. This interpolation is not straightforward since the heights of the bottom and top of the overlap correction region are different for each temperature.

The solution for interpolation of the correction function between temperatures is to first normalize the height variable relative to the top and bottom of the incomplete overlap region. This normalized height variable is then

$$Z_N = \frac{Z - Z_B}{Z_T - Z_B},$$

where Z_B is the height of the bottom of the overlap region and Z_T is the height where complete overlap is achieved. Each overlap function, at each temperature, is defined for values of Z_N between zero and unity. Figure 15 shows the overlap fraction as a function of normalized height for two temperatures. Table 4 gives the values at each temperature used in testing. The inverse of the overlap fraction is the correction function and this is given in Table 5.

At each temperature there are unique values of Z_B and Z_T. At temperatures that are not equal to those used in testing, the values of Z_B and Z_T can be determined by interpolation. There are three interpolations: one for the overlap or correction function in normalized height, another for the values of Z_B and Z_T, and then a final interpolation to map the correction function onto the regular height above ground in the range from Z_B and Z_T. This can then be applied to the data by multiplication.

9 PHOTON COUNTING LINEAR DYNAMIC RANGE

Determination of the linear dynamic range in the signal acquisition is of vital importance for interpreting the lidar atmospheric measurements. At high signal strengths the photon counting detection will not respond in the same way as it does for weaker signals. For example, if the optical signal is doubled, the recorded electrical signal will not increase by the same factor. For photon counting this occurs because the individual pulses in the electrical signal are of finite width. At count rates greater than 5 MHz, photons arrive often enough that the associated electrical pulses overlap. The result is that two photons can be counted as only one (loss), or two pulses that would individually not be of sufficient amplitude to be detected may combine to get counted (gain). This will occur at the lowest heights, where the backscatter signal is greatest.

A straightforward test of photon counting linearity involves comparing the photon counting and analog signals from the photomultiplier (detecting the 532 nm wavelength). The ratio of these signals will be constant in the linear range and it will be reduced (or enhanced) at high count rates when the detection is nonlinear. The deviation from the constant value will be a measure of the departure from linearity. The value of this ratio will be used to correct for the detection non-linearity.

Figure 16 shows a ratio of the signals recorded by photon counting and analog acquisition, as a function of the photon counting rate. This illustrates the reduction in the recorded signal at each recorded photon count rate. The photon counting was linear up to 5 MHz; nonlinearity reduced the photon counting signal by a factor of 0.9 at a recorded count rate of 10 MHz, and by a factor of 0.67 at 20 MHz. The inverse of the ratio in Figure 16 is a correction for nonlinearity. Table 6 gives the values of the reduction ratio and the correction for various photon counting rates.

This method will also provide a test of the detector function during normal measurements on Mars and will indicate if there are changes in the function of the detectors or circuitry.

10 LIDAR CALIBRATION

The equation that describes a Lidar backscatter signal as a function of height can be written as

$$S(z) = C \times \beta(z) \times 1/z^2 \times T(z)^2 \quad (MHz)$$

$\beta(z)$ is the lidar backscatter coefficient and this represents the fraction of optical energy scattered back into the lidar receiver per unit length and per unit solid angle. $T(z)$ is the transmittance through the atmosphere. This can be expressed in terms of optical depth as $T = \exp(-OD)$. The optical depth is expressed in terms of the extinction coefficient as $OD = \int \alpha \, dz$. The lidar equation has two parameters, β and α, that relate to the properties of material in the atmosphere. A standard method for solving the lidar equation was described by Klett (1981).

The constant C takes into account factors that include the laser pulse energy, area of the receiver aperture, transmittance of the receiver optics, and the quantum efficiency of the PMT detector in photon counting mode. This has been determined to have a value of 4×10^{12} sr m^3 by comparing the recorded backscatter signal to what is expected from the atmosphere based on measurement data from weather balloons (radiosondes). The lidar signal calculated for molecular backscatter only is shown in Fig. 10 and this matches the measured signal where there is no cloud.

11 LIDAR SENSITIVITY TO BACKGROUND SKYLIGHT

The signal shown in Fig. 10 was obtained just before 5 am during equinox at Ottawa and there was essentially zero background skylight to detect within the 1 nm optical bandwidth of the Phoenix lidar. This will not be the case on Mars since the the Phoenix mission will take place during the summer and the landing site will be at high latitude. The sun will not set for most of the mission. The background skylight will be the limiting factor and this must be taken into account in an assessment of the performance of the Phoenix lidar.

The sensitivity of the Phoenix lidar to background skylight was determined by comparison with the background signal measured simultaneously with the York Lidar, which was previously calibrated. It was determined that the Phoenix lidar has a photon counting background skylight sensitivity of 0.4 MHz per unit of radiance in $W/m^2/\mu m/sr$.

An atmospheric radiative transfer model (Moores et al. 2007) has been applied to estimate the background light intensity on the surface of Mars. With a dust optical depth of 0.2 and at maximum solar elevation during the mission, the background skylight intensity was estimated to be 10.2 $W/m^2/\mu m/sr$. The skylight intensity at the minimum solar elevation that will be encountered during the mission was estimated to be 1.5 $W/m^2/\mu m/sr$. The corresponding background count rates recorded by the Phoenix lidar are a maximum of 4.0 MHz and a minimum of 0.6 MHz.

12 MINIMUM DETECTABLE SIGNAL

Photon counting will be used for detecting the very weak signals from high clouds. The minimum detectable signal level is determined by the statistical fluctuations (or uncertainty) inherent in the photon counting process. The statistical nature of Photon counting is described by the Poisson distribution in which the standard deviation is equal to the square root of the mean value. The magnitude of this statistical noise in the recorded signal will be determined by the background light level. The signal from clouds must be greater than the standard deviation of the statistical fluctuations (or uncertainty) in order to be detectable.

The standard deviation in the background count rate is shown in Fig. 17 for temporal/spatial integrations of 15 min/ 500 m, 1 min/ 50 m, and 10 seconds/ 50 m. Figure 17a shows the results for maximum solar elevation, while Fig 17b shows the results for minimum solar elevation.

13 LIDAR PERFORMANCE FOR DETECTING HIGH CLOUDS

The performance of the Phoenix Lidar will be demonstrated here in terms of its ability to detect clouds. The design requirement (3117) in this respect states that the lidar must be capable of detecting a cloud of optical depth 0.05 at a height of 20 km when the dust at lower heights has an optical depth of 0.2.

It is fortuitous that the cirrus cloud at heights between 9 km and 11 km in Fig. 10 has an optical depth of 0.05. The ratio of the signal above the cloud to the calculated molecular backscatter signal is 0.9. The reduction from the value of unity is due to the attenuation through the cloud. The two-way transmittance through the cloud is 0.9. From this value the optical depth of the cloud is determined to be 0.05. The peak signal from this cloud will be used as a basis for computations to determine the performance for cloud detection.

The lidar equation (Sec. 7) was used to calculate the peak signal from a cloud with optical properties and thickness equivalent to the cloud in Fig. 10, but situated at heights from ground to 20 km. It was assumed that dust below the cloud had an optical depth of 0.2, regardless of the height of the cloud. This is shown in Figure 17. It is seen that for maximum solar elevation the background standard deviation is about half of the peak signal from the cloud at 20 km when using the longest spatial/temporal averaging. The requirement for cloud detection up to 20 km is thus satisfied.

The difference between midnight and midday measurements is also demonstrated in Fig. 17. At maximum solar elevation and temporal/spatial averaging of 1 min/50 m, the cloud signal is equal to the background standard deviation at a height of 8.5 km. At minimum solar elevation the cloud signal equals the statistical noise at a height of 13.5 km.

14 ESTIMATION OF ICE WATER CONTENT FROM LIDAR MEASUREMENTS

The main goal of the mission is to investigate the existence of water on Mars. Although not currently provided as a data product, one aspect that the lidar can address is the ice water content (IWC) of clouds. A method has been developed to derive IWC from the lidar measurements. This has involved a combination of lidar remote sensing and airborne in situ sampling of ice crystals in cirrus clouds. The data from three separate measurement campaigns has been employed. The ACTIVE campaign at Darwin Australia in 2006 involved the York Lidar on board a Twin Otter aircraft flying below clouds while in situ measurements were obtained from the Egrett. Another Darwin measurement campaign called EMERALD-2 in 2002 involved a similar arrangement of aircraft with a King Air aircraft carrying an upward looking lidar that was an early version of the York Lidar. The EMERALD-1 campaign also employed the same equipment, but this was carried out at Adelaide Australia. The measurements from the EMERALD-1 campaign were best suited for the Phoenix lidar characterization since it was a greater priority to keep the aircraft aligned for simultaneous measurements. Dr. Jim Whiteway (author of this report) was the overall Principal Investigator for the Emerald campaigns. The experimental concept is illustrated in Fig. 18. Figure 19 shows photographs of the aircraft and instruments. An example of the combination of in situ ice crystal sampling and lidar measurements is shown in Fig. 20.

The basis of the method is to relate IWC to the extinction coefficient derived from the lidar measurements. The extinction coefficient is the fractional reduction of the laser pulse energy per unit length. This can also be stated as the effective cross-sectional area of scattering material per unit volume. If the relationship between area and volume is known for the ice crystals then one can determine the mass of water ice per unit volume – the ice water content (IWC). This would be straightforward for spherical water droplets, but more complicated for non-spherical ice crystals. With simultaneous lidar and in situ measurements it has been possible to determine an empirical relationship between optical extinction and IWC.

Figure 21 shows a scatter plot of the extinction derived from lidar measurements and the IWC derived from the in situ measurements. The fit to this data represents the empirical relationship that will be used to calculate the IWC from lidar measurements of extinction. A reasonable estimate of the uncertainty is the standard deviation of the relative difference between the fit and the actual measurements in Fig. 21. This uncertainty is 15 %.

The limited number of data points in Fig. 21 reflects a careful control of the data. The measurement data were used only if it was certain that the lidar and the Egrett in situ instruments were sampling the same volume of air. Instances where there was a very large variability in the cloud IWC were also removed so that the averages were representative.

The extinction coefficient was derived from the lidar measurements using the method described by Klett (1981). The ice water content was determined by integrating the measured ice crystal size distribution. The two instruments that were used for the in situ measurements are listed in Tabel 7. The Forward Scatter Spectrometer Probe (FSSP) was used for ice crystals with maximum dimension smaller than 40 micrometers. The Cloud Particle Imager (CPI) was used for measuring the concentration and size of particles with maximum dimension greater than 40 micrometers. The analysis of the in situ cloud particle measurements was described in Gallagher et al. (2005).

Figure 21 includes measurements in a wide range of atmospheric conditions and microphysical characteristics. This is demonstrated in Figure 22, where each data point is classified according to position within the cloud, pressure, temperature, average crystal radius, and number density. There is no obvious dependence on either of these factors within the range of measurements acquired. The clouds in the Martian atmosphere will have similar and colder temperatures, but pressures that are lower by a factor of 100.

Figure 23 shows the lidar signal and derived extinction and IWC at one time in the flight on 11 Sept 2001. The in situ measurement of IWC is also shown with error bars that represent the standard deviation over the averaging period. Figure 24 shows the lidar and in situ IWC over the entire flight. The relative agreement is very good considering that there is a large variability in cloud IWC and the aircraft could not be aligned perfectly.

Figure 25 illustrates four steps in the analysis of lidar signals and the estimation of ice water content from the lidar measurements of a cirrus cloud with the actual flight model of the Phoenix Lidar. The measurements are shown in Fig. 10. Figure 25a is the ratio of the recorded backscatter to the calculated molecular backscatter. This is referred to as the attenuated backscatter ratio since the effect of extinction has not been taken into account. The cloud backscatter coefficients can be estimated from the backscatter ratio since the molecular backscatter coefficient is well known, and this is shown in Fig. 25b. The profile of extinction coefficient, calculated employing the method of Klett (1981), is shown in Fig. 25c. Figure 25d shows the IWC calculated from the extinction coefficient profile in Fig. 6c using the IWC-extinction relationship from Fig 21.

The capability to derive IWC from the lidar measurements on Mars will be of vital importance for investigating the transport of water through the atmosphere, though several additional challenges present themselves. Most notable is the poorly known optical properties for aeolian Martian dust, which would be substituted for the molecular atmosphere in the above analysis. Investigations are ongoing, however, involving simultaneous lidar and aircraft in situ measurements in order refine the parameterization and to quantify the uncertainty in deriving cloud IWC from lidar measurements in a dusty atmosphere such as Mars.

15 APPLICATION OF COLOUR RATIO

The lidar colour ratio, or ratio of 1064 and 532 nm signals, is not currently a standard data product, but is included here for completeness.

A field campaign involving the York Lidar operating from the ground and in situ measurements of airborne desert dust has been conducted in the Australian interior during November 2007. On of the goals of this campaign was to relate the lidar colour ratio to microphysical properties. The analysis is ongoing and this section will be completed before

16 REFERENCES

Boynton et al., Distribution of Hydrogen in the Near Surface of Mars: Evidence for Subsurface Ice Deposits, *Science,* vol. 297, no. 5578, pp. 81 – 85, 5 July 2002.

Heymsfield, A. J., D. Winker, G. van Zadelhoff, Extinction-ice water content-effective radius algorithms for CALIPSO, *Geophysical Research Letters,* volume 32, L10807, doi:10.1029/2005GL022742, 2005.

Klett J., Stable analytical inversion solution for processing lidar returns, *Applied Optics*, vol. 20, pages 211-220, 1981.

Lemmon, M, et al., The Phoenix Surface Stereo Imager (SSI) investigation, *Journal of Geophysical Research (Phoenix special issue), submitted 2007.*

Leovy, C., Weather and climate on Mars, *Nature,* volume 412, pp. 245-249, 12 July 2001

Moores, J.E., P.H. Smith, R. Tanner, A. C. Schuerger, and K. J. Venkateswaran,The shielding effect of small scale Martian surface geometry on ultraviolet flux. *Icarus, in review,* 2007.

Measures, R. M., Laser remote sensing: Fundamentals and applications, pp 510, Wiley and Sons, New York, 1984.

Neumann, G. A., D. E. Smith, M. T. Zuber, Two years of clouds detected by the Mars Orbiter Laser Altimeter, *Journal of Geophysical Research,* volume 108(E4), 5023, doi:10.1029/2002JE001849, 2003.

Newman, C. E., S. R. Lewis, P. L. Read, Modeling the Martian dust cycle 1. Representations of dust transport processes, *Journal of Geophysical Research,* volume 107(E12), 5123, doi:10.1029/2002JE001910, 2002.

Pathak J. D.V. Michelangali, L. Komguem, J. Whiteway, L. Tamppari, Simulating Martian boundary layer water ice clouds and the lidar measurements for the Phoenix mission, *Journal of Geophyical. Research (Phoenix special issue), submitted 2007.*

Smith, P. et al., Scientific Overview of the Phoenix Mission, *Journal of Geophysical Research (Phoenix special issue), submitted 2007.*

Taylor, P. et al., Meteorology Station MET on the Phoenix Mars Lander: Pressure, Temperature and Wind Speed, *Journal of Geophysical Research (Phoenix special issue), submitted 2007.*

Whiteway et al., Lidar on the Phoenix Mars Mission, *Journal of Geophysical Research (Phoenix special issue), submitted 2007.*

Zent,A. et al., TECP and Humidity, *Journal of Geophysical Research (Phoenix special issue), submitted 2007.*

APPENDIX A. LIST OF TABLES

Table 1: Basic characteristics of the Phoenix Lidar.

Transmitter		
Laser	Nd: YAG Diode pumped	
Wavelengths	1064 nm	532 nm
Pulse repetition rate	100 Hz	100 Hz
Pulse energy	0.3 mJ	0.4 mJ
Divergence	0.25 mrad	0.25 mrad
Emitted line width	0.25 nm	0.25 nm
Receiver		
Telescope	10 cm diameter	
Field of View	2 mrad	1.5 mrad
Spectral width	2 nm	1 nm
Detector	Silicon APD	PMT
Signal recording	Analog:14 bit ADC	Analog: 14 bit ADC + Photon Counting
Sampling frequency	30 MHz (5 m)	30 MHz (5 m)
Total Mass	6 kg	
Maximum Power	30 W	

Table 2. Thermal distortion: The angular separation between the transmitter output and the receiver field of view axis at various temperatures. Positive angles represent the transmitter pointing away from the receiver.

Temperature (^{o}C)	**Angle (mrad)**
-40	+ 0.9
-30	+ 0.2
-20	- 0.1
-10	-0.25
0	-0.5

Table 3. Bottom and top heights for the incomplete overlap region at the temperatures that were used in testing.

Temperature [°C]	z_{Bottom} [m]	z_{Top} [m]
-40	125.0	1170.0
-38	122.2	960.0
-32	116.4	690.0
-25	111.2	540.0
-18	98.3	330.0
-10	72.4	150.0

Table 4. Fractional overlap as a function of normalized height at the temperatures used in testing.

$\frac{Z - Z_{Bottom}}{Z_{Top} - Z_{Bottom}}$	Temperature [° C]					
	-40	-38	-32	-25	-18	-10
0.00	-	-	-	-	-	-
0.01	0.01	0.01	0.01	0.02	0.03	0.03
0.05	0.03	0.04	0.06	0.11	0.14	0.11
0.10	0.12	0.14	0.18	0.25	0.28	0.21
0.15	0.29	0.31	0.34	0.41	0.41	0.31
0.20	0.43	0.45	0.50	0.55	0.53	0.41
0.25	0.52	0.56	0.60	0.65	0.65	0.48
0.30	0.72	0.65	0.67	0.72	0.72	0.56
0.35	0.77	0.76	0.73	0.75	0.77	0.63
0.40	0.80	0.82	0.78	0.79	0.80	0.71
0.45	0.83	0.87	0.83	0.83	0.83	0.76
0.50	0.85	0.89	0.89	0.87	0.84	0.81
0.55	0.87	0.90	0.93	0.94	0.85	0.86
0.60	0.89	0.92	0.95	0.94	0.87	0.91
0.65	0.91	0.94	0.96	0.95	0.88	0.93
0.70	0.92	0.95	0.96	0.97	0.91	0.94
0.75	0.95	0.96	0.97	0.99	0.93	0.95
0.80	0.96	0.98	0.97	0.99	0.95	0.96
0.90	0.98	0.99	0.98	0.99	0.96	0.98
1.00	1.00	0.99	0.99	0.99	1.01	1.00

Table 5. Overlap correction factor as a function of normalized height at the temperatures used in testing.

$\frac{Z - Z_{Bottom}}{Z_{Top} - Z_{Bottom}}$	Temperature [° C]					
	-40	-38	-32	-25	-18	-10
0.00	-	-	-	-	-	-
0.01	194.38	126.43	80.28	43.54	30.79	32.57
0.05	39.98	26.79	16.84	9.18	6.97	9.08
0.10	8.27	7.03	5.59	4.04	3.57	4.77
0.15	3.50	3.23	2.92	2.45	2.45	3.24
0.20	2.32	2.22	2.02	1.81	1.88	2.45
0.25	1.92	1.77	1.67	1.53	1.55	2.07
0.30	1.40	1.54	1.49	1.39	1.38	1.80
0.35	1.30	1.31	1.37	1.33	1.30	1.58
0.40	1.25	1.22	1.28	1.26	1.25	1.42
0.45	1.21	1.15	1.21	1.20	1.20	1.32
0.50	1.17	1.13	1.12	1.15	1.19	1.24
0.55	1.15	1.11	1.08	1.06	1.18	1.16
0.60	1.12	1.09	1.05	1.06	1.16	1.10
0.65	1.10	1.07	1.05	1.05	1.13	1.08
0.70	1.08	1.05	1.04	1.03	1.10	1.07
0.75	1.05	1.04	1.03	1.01	1.08	1.05
0.80	1.04	1.03	1.03	1.01	1.06	1.04
0.90	1.02	1.01	1.02	1.01	1.04	1.02
1.00	1.00	1.01	1.01	1.01	0.99	1.00

Table 6. Nonlinear photon counting signal reduction factor (left) correction factor (middle) for count rates (right) up to 30 MHz.

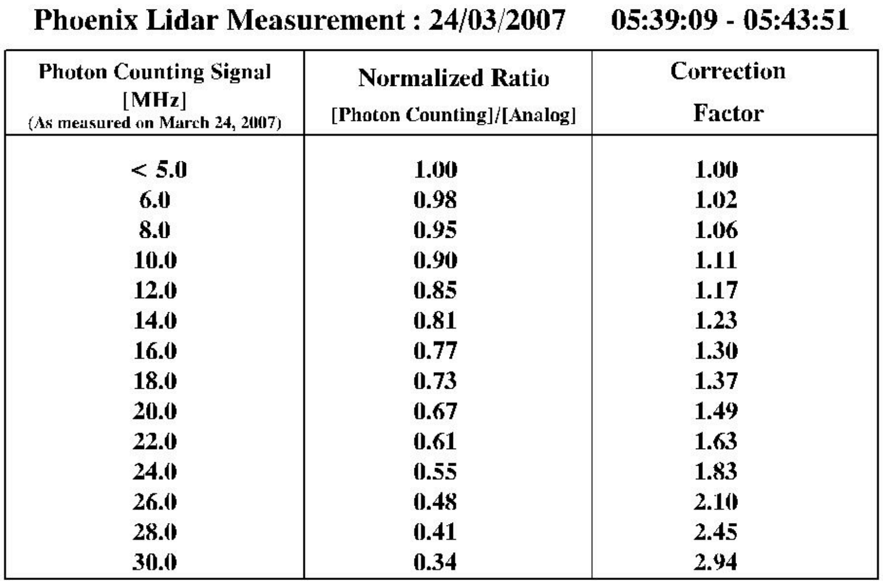

Phoenix Lidar Measurement : 24/03/2007 05:39:09 - 05:43:51

Photon Counting Signal [MHz] (As measured on March 24, 2007)	Normalized Ratio [Photon Counting]/[Analog]	Correction Factor
< 5.0	1.00	1.00
6.0	0.98	1.02
8.0	0.95	1.06
10.0	0.90	1.11
12.0	0.85	1.17
14.0	0.81	1.23
16.0	0.77	1.30
18.0	0.73	1.37
20.0	0.67	1.49
22.0	0.61	1.63
24.0	0.55	1.83
26.0	0.48	2.10
28.0	0.41	2.45
30.0	0.34	2.94

Table 7. Cloud particle in situ measurements on the Egrett aircraft

Measurement	*Instrument*	*Institute*
PArticle concentration and size distribution ($0.3 < D_p < 40$ µm)	Forward Scatter spectrometer probe (FSSP)	University of Manchester
Cloud particle/ice CCD images Size distribution ($10 < D_p < 2{,}300$ µm)	SPEC Cloud Particle Imager CPI-230.	University of Manchester

APPENDIX B. LIST OF FIGURES

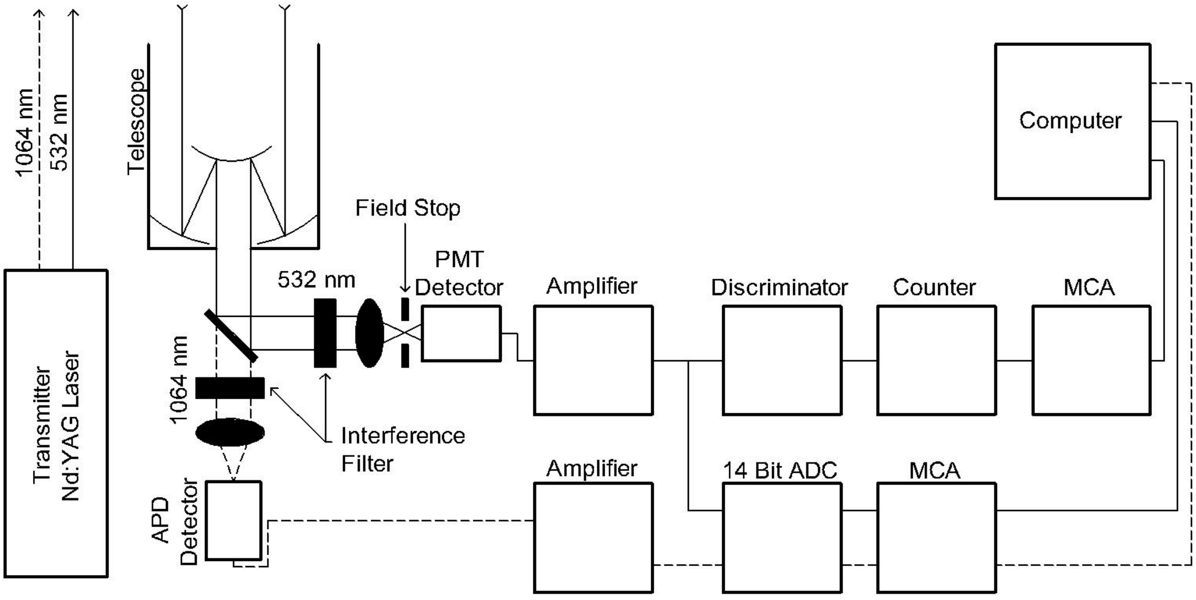

Figure 1: Schematic diagram of the Phoenix Lidar.

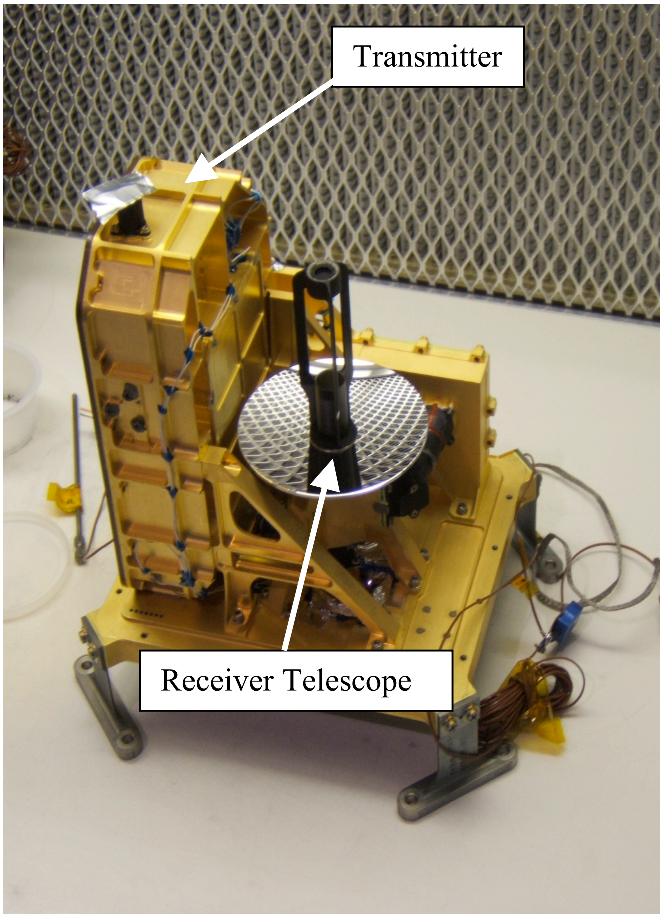

Figure 2. Photograph of the Phoenix Lidar with the cover removed.

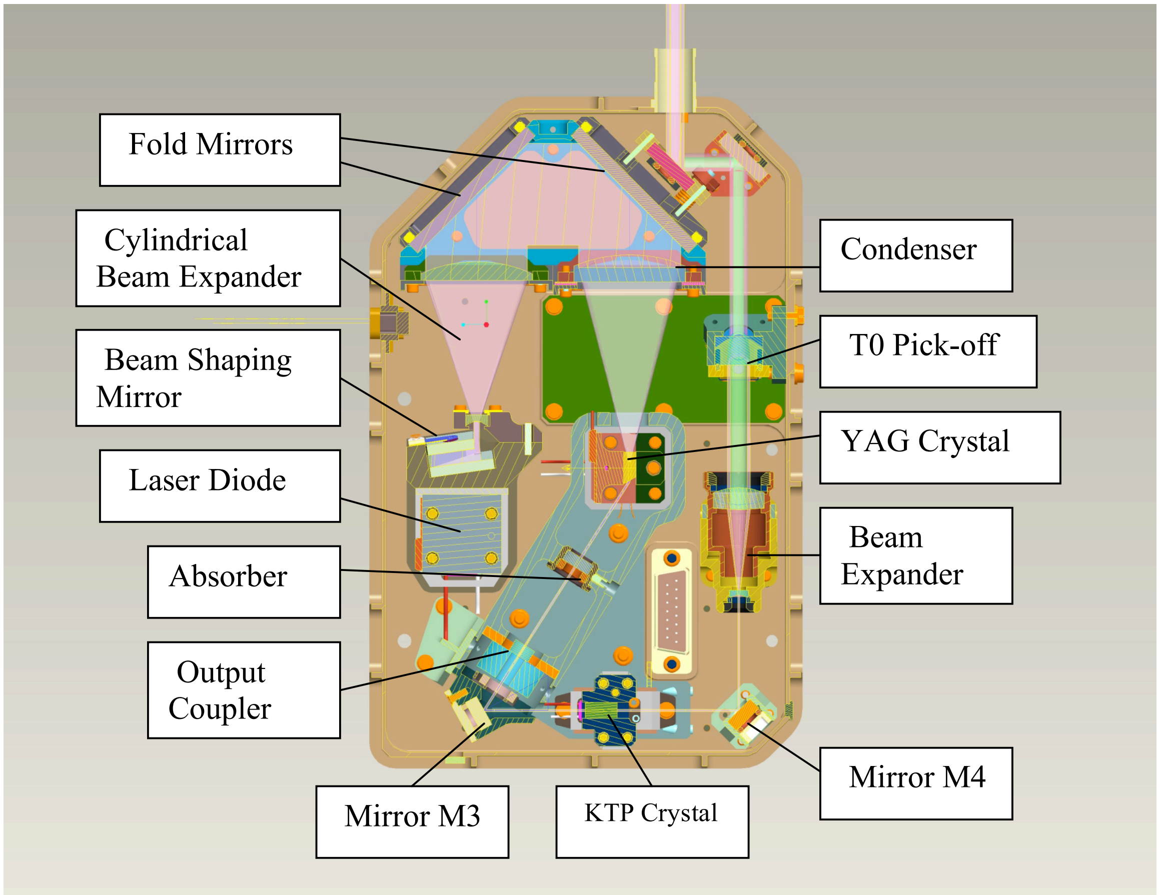

Figure 3. Drawing of the Phoenix Lidar laser transmitter.

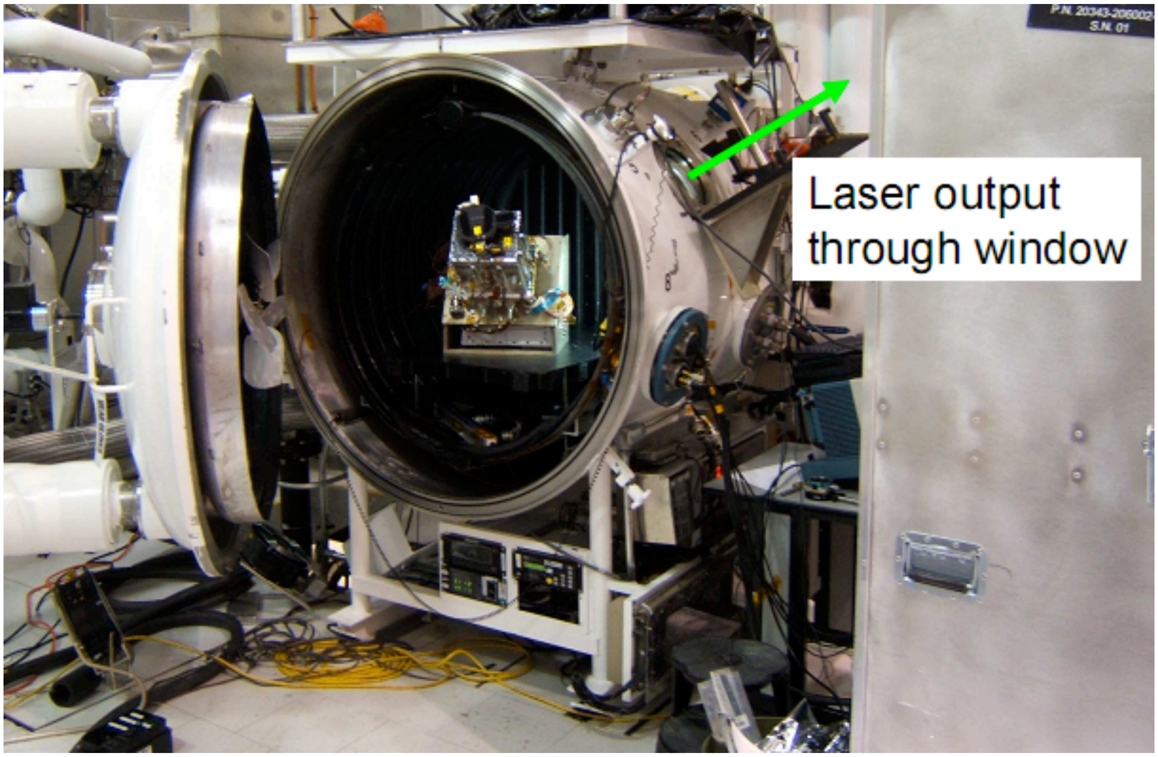

Figure 4. The Phoenix lidar installed in the thermal vacuum chamber for testing at the CSA David Florida Laboratory (March 2006).

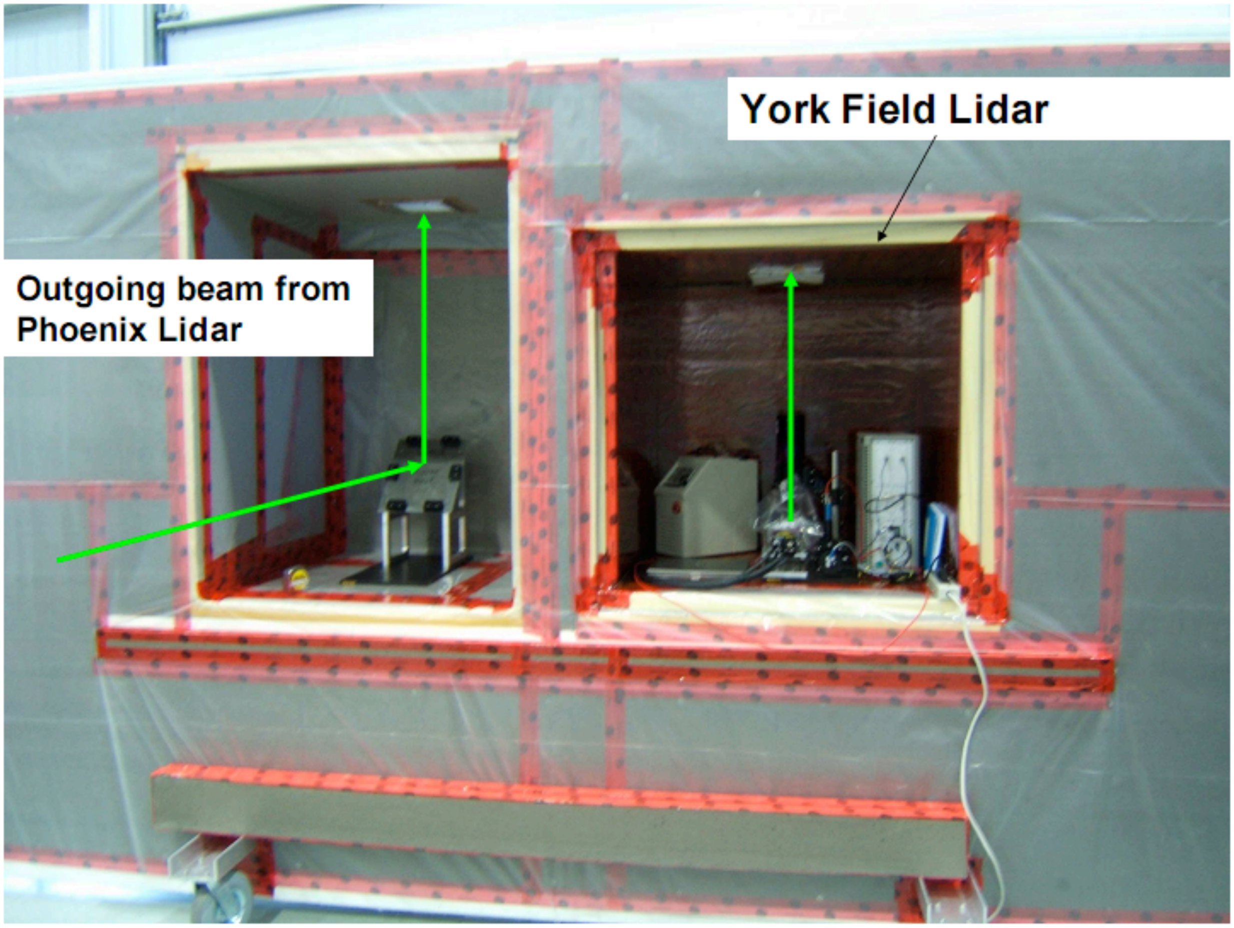

Figure 5. Wall compartments installed at the DFL laboratory for upward viewing of the atmosphere from inside the clean room.

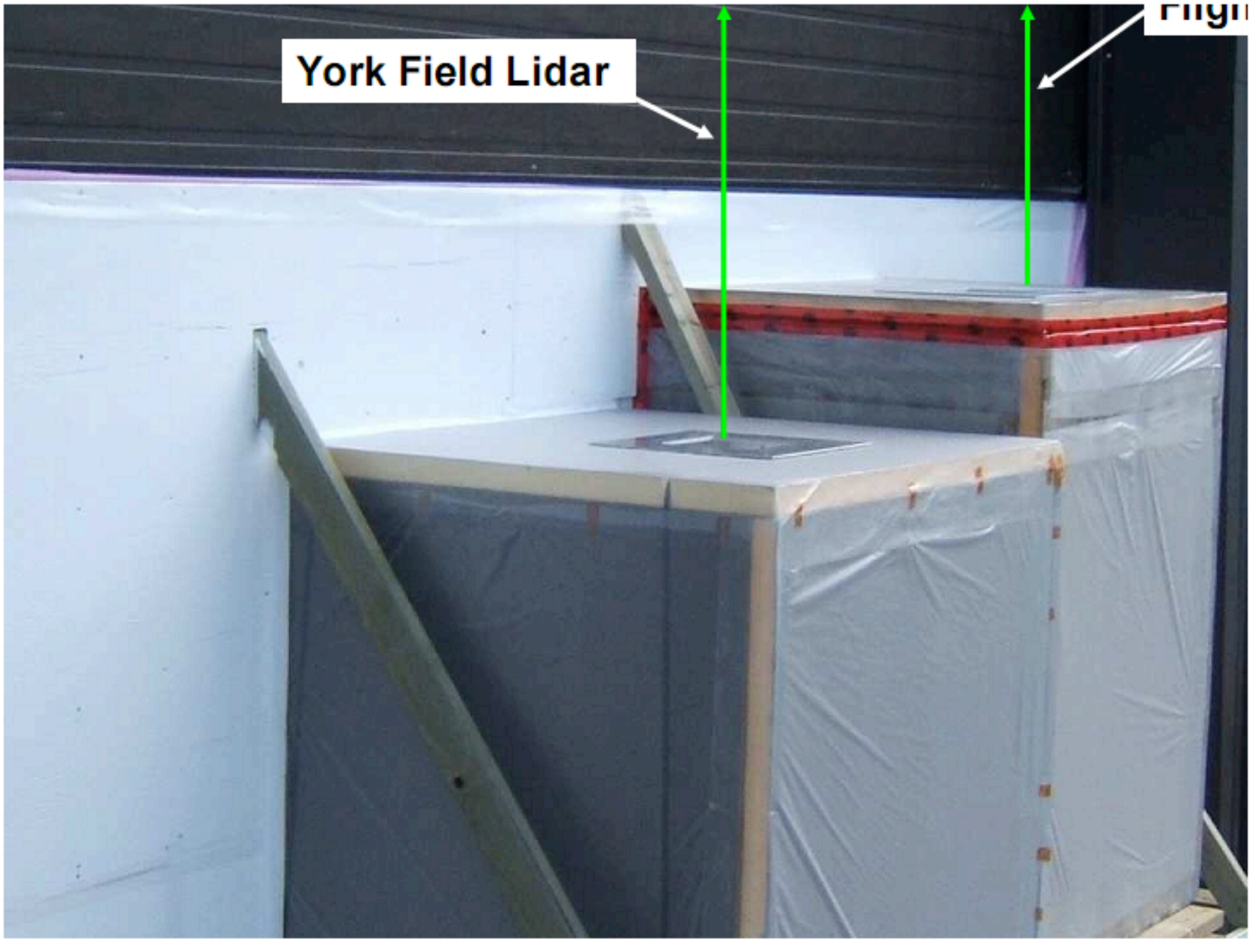

Figure 6. Outdoor side of the wall compartments at DFL for upward viewing of the atmosphere from inside the clean room.

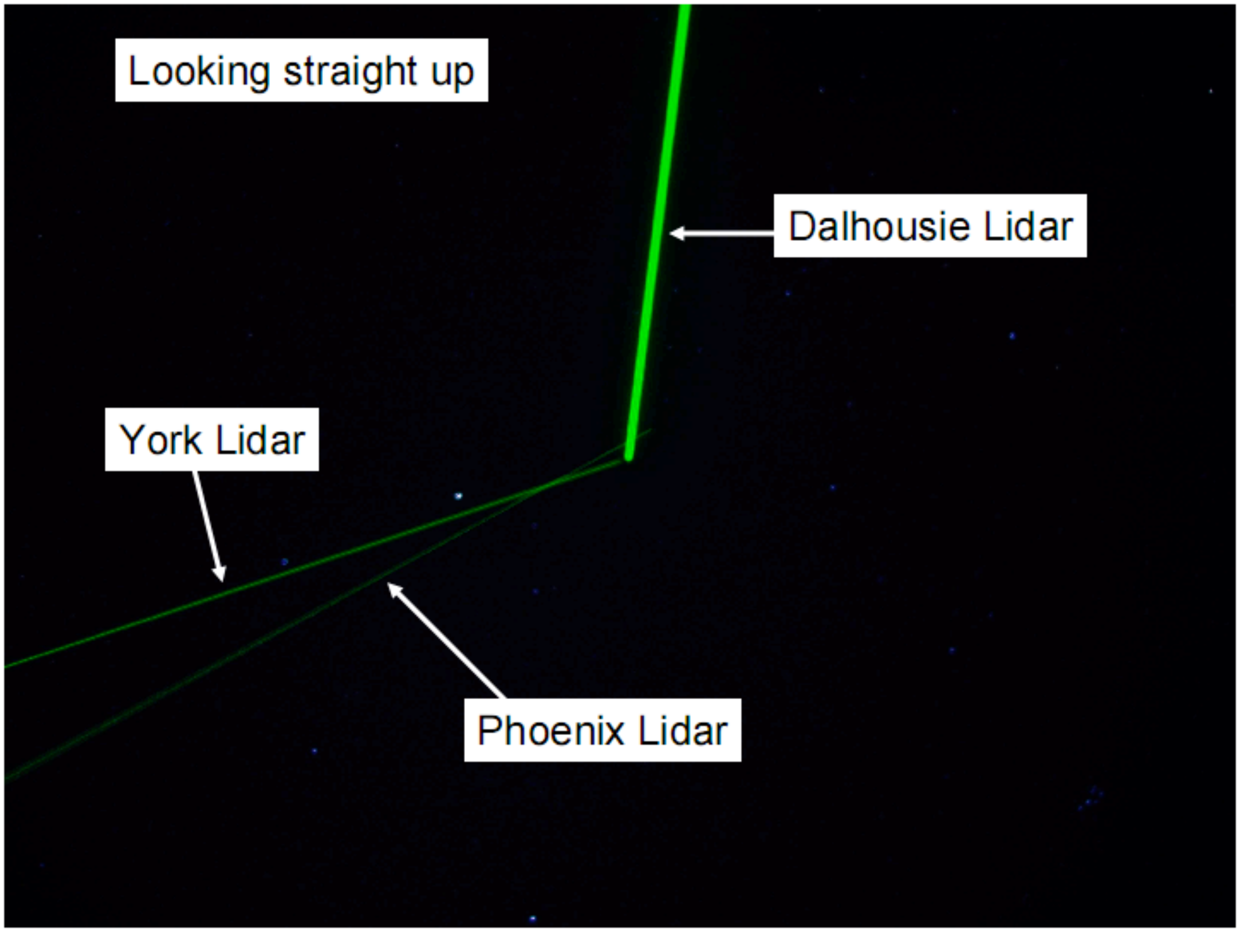

Figure 7. Upward view from DFL with laser beams from the Phoenix lidar, the York Lidar, and the Dalhousie Lidar.

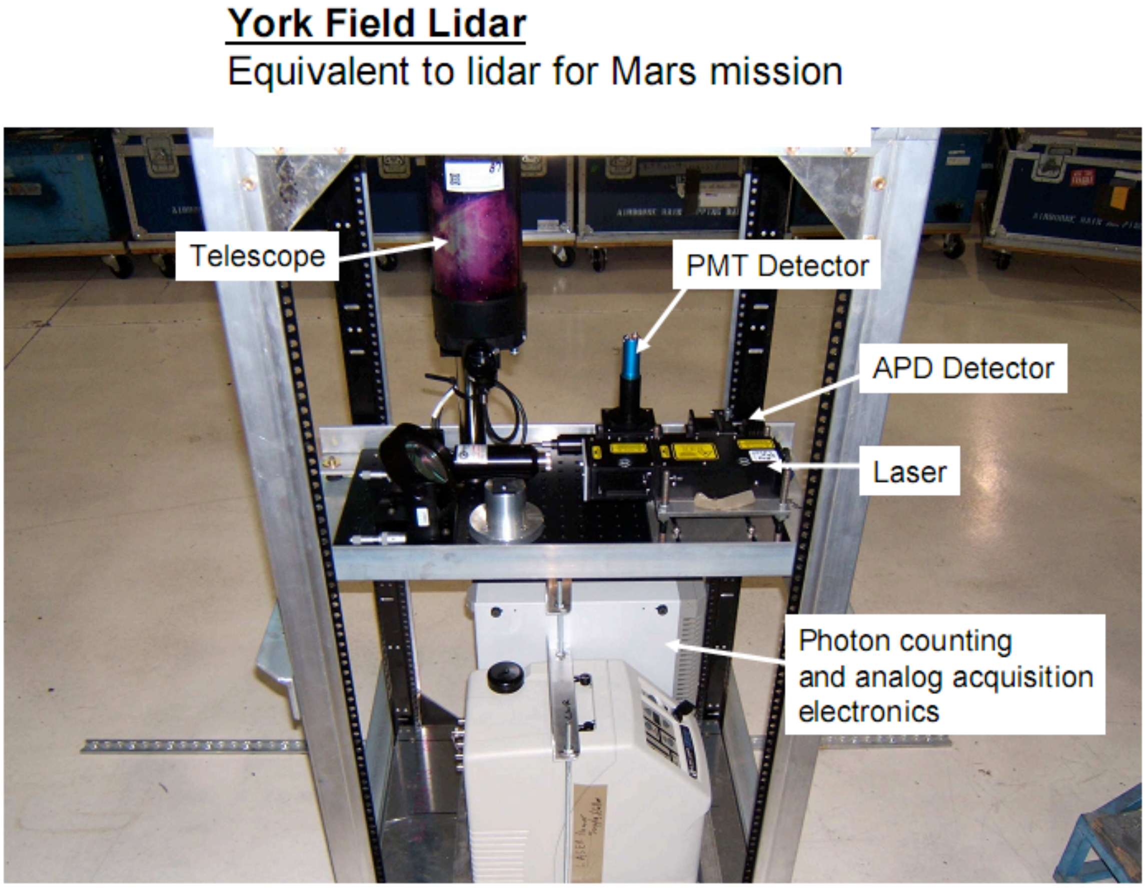

Figure 8. The York Lidar integrated in a rack for installation on the Twin Otter aircraft.

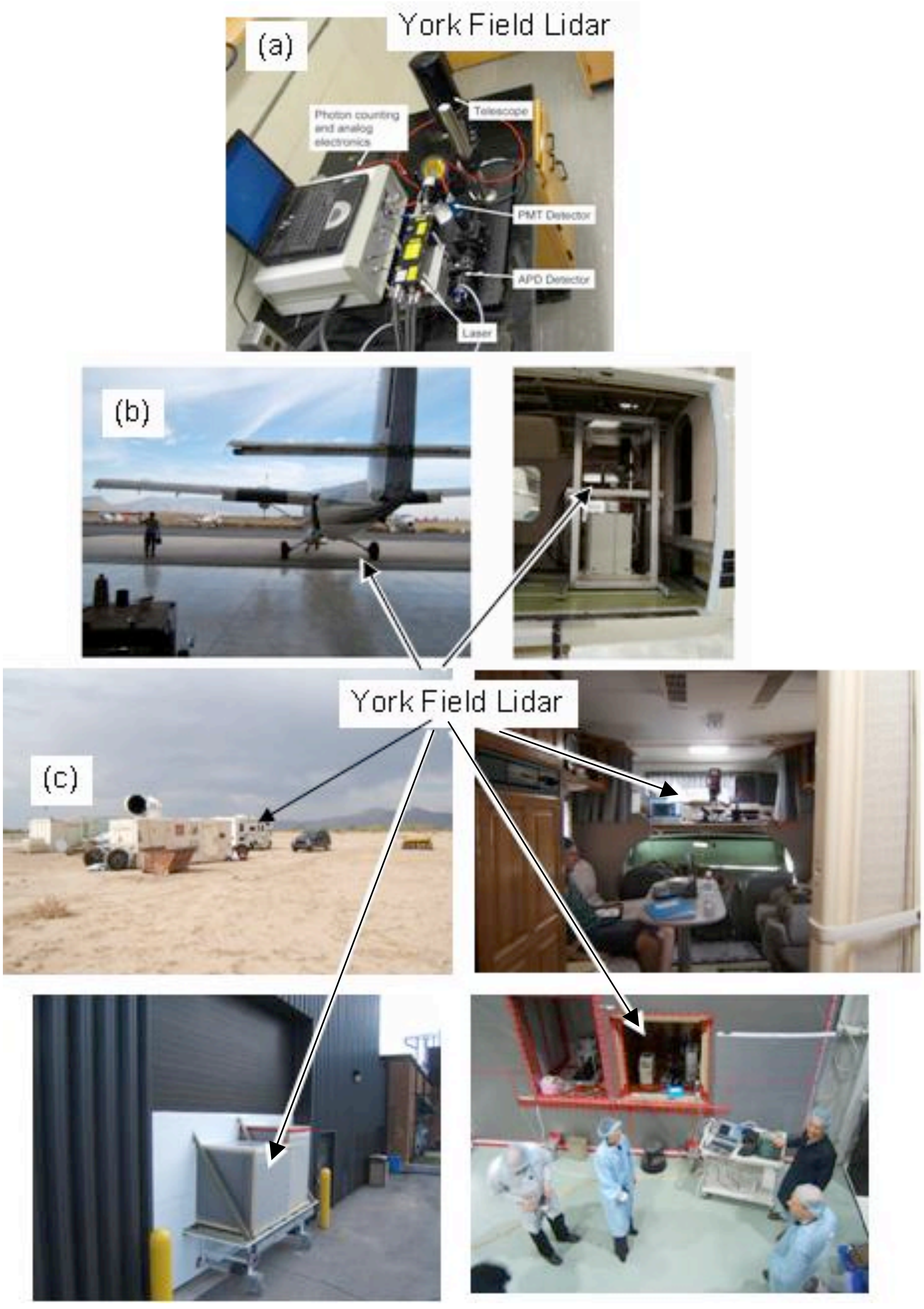

Figure 9: The York Lidar in various deployments for characterization of the Phoenix lidar: (a) testing at York University; (b) installation on the Twin Otter aircraft for the ice cloud campaign at Darwin, Australia (January 2006); (c) installation in an RV for the desert dust campaign at Eloy, Arizona (June 2006). (d) installation at DFL, Ottawa, for side-by-side testing (November 2006 to March 2007).

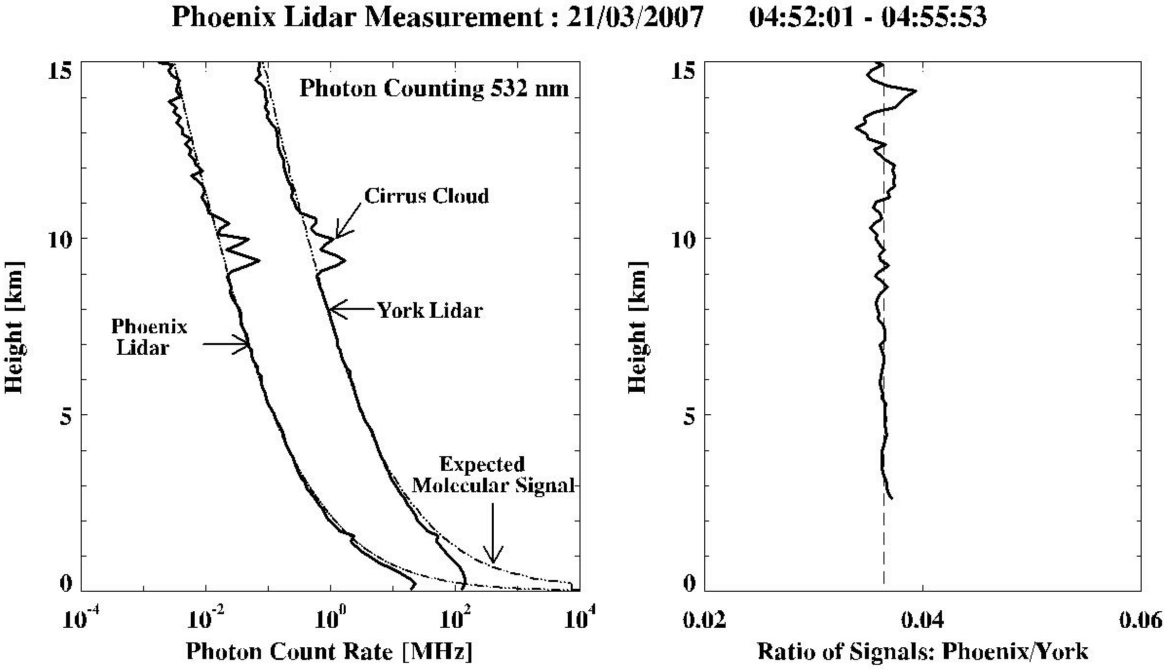

Figure 10. Atmospheric measurements obtained simultaneously with the Phoenix lidar and the York Field Lidar at the wavelength of 532 nm. The Phoenix Lidar was operating inside the thermal vacuum chamber in an environment consisting of carbon dioxide at a pressure of 8 Torr and a temperature of -70° C. The Phoenix lidar internal chassis temperature was -36° C.

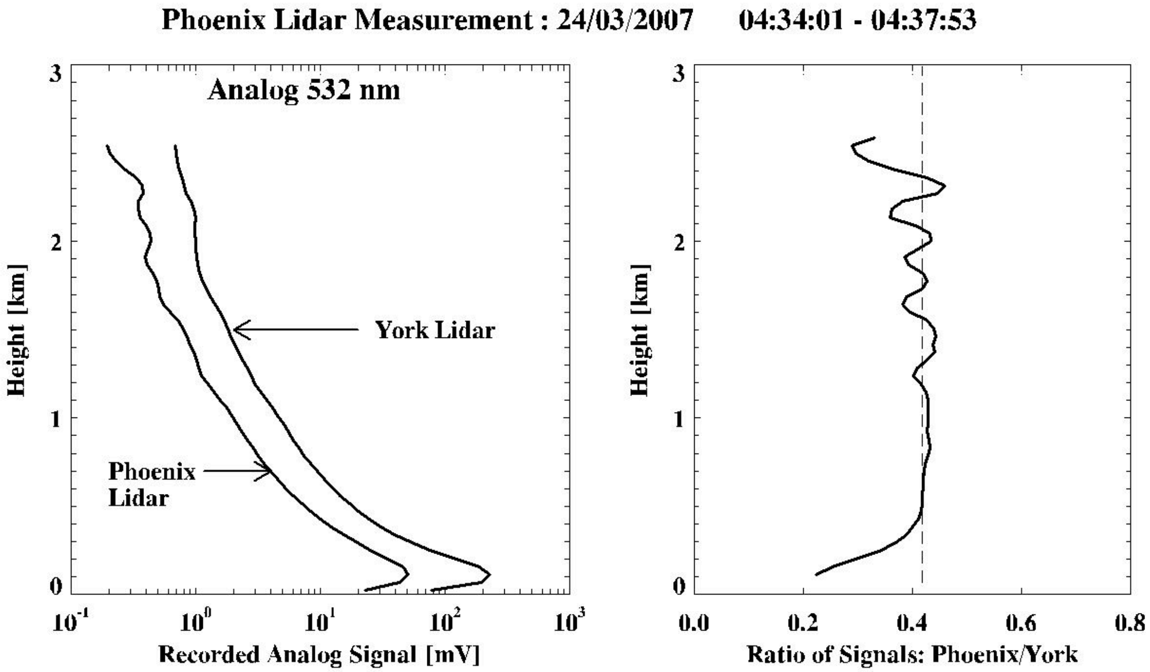

Figure 11. Atmospheric measurements obtained simultaneously with the Phoenix lidar and the York Field Lidar at the wavelength of 532 nm and recorded by analog to digital conversion. The Phoenix Lidar was operating inside the thermal vacuum chamber in an environment consisting of carbon dioxide at a pressure of 8 Torr and a temperature of -70° C. The Phoenix lidar internal chassis temperature was -30° C.

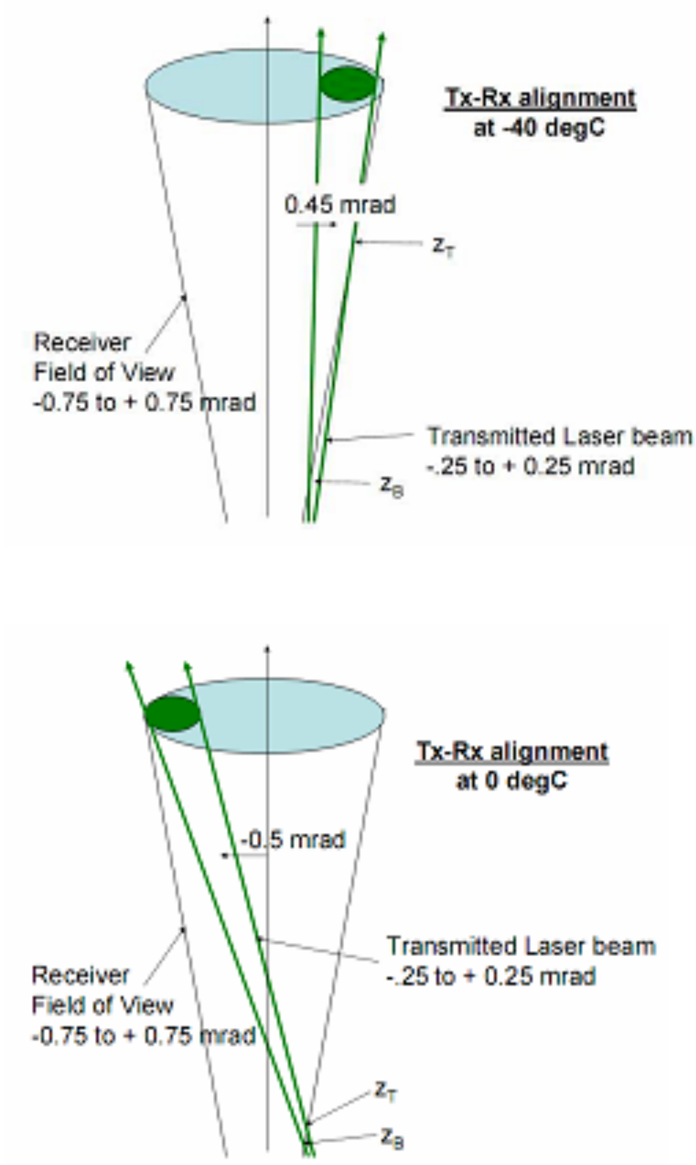

Figure 12. Illustration of the transmitter-Receiver alignment geometry, and how it changes with temperature. It is also seen how the extent of the incomplete overlap region, between heights Z_B and Z_T, is sensitive to changes in alignment and thus also temperature.

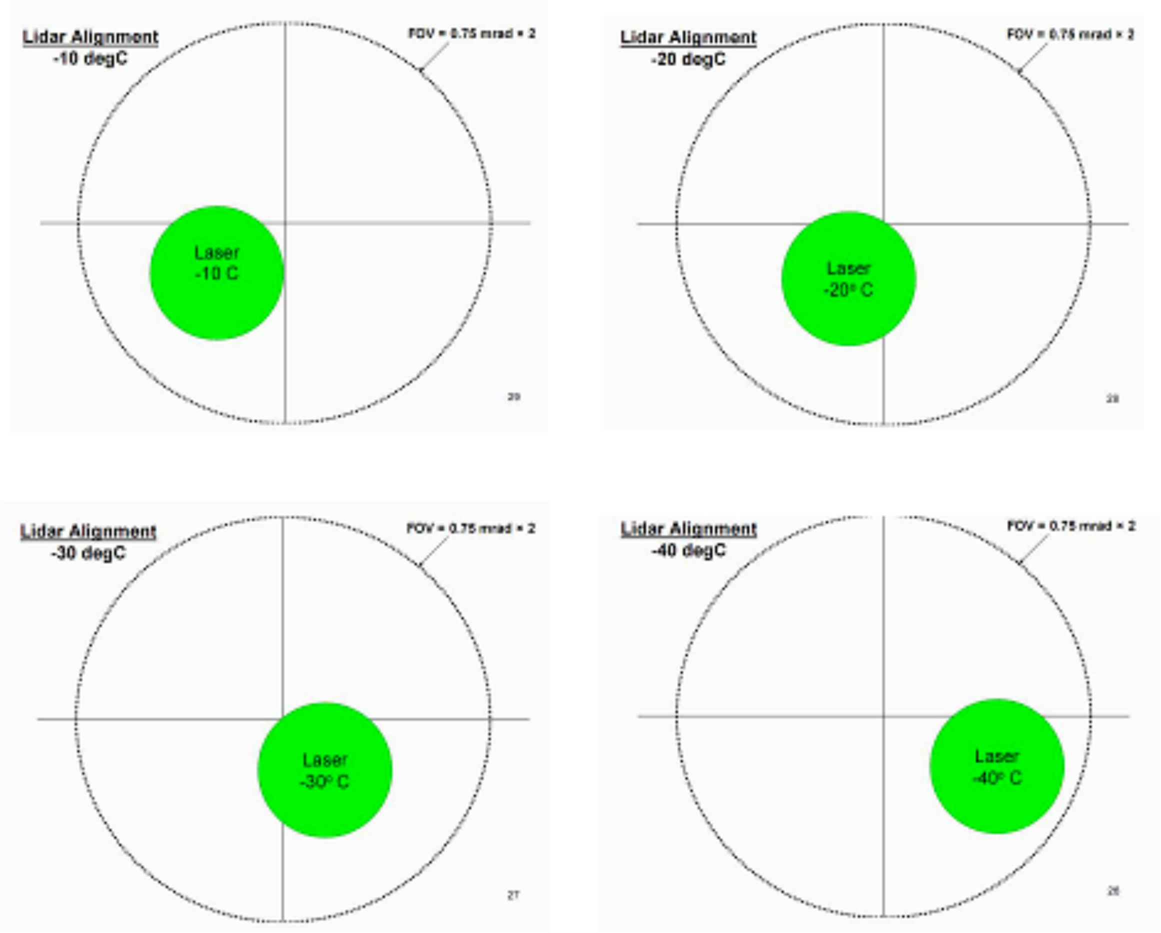

Figure 13. Illustration of position of the laser output relative to the telescope field of view at various temperatures (looking upward).

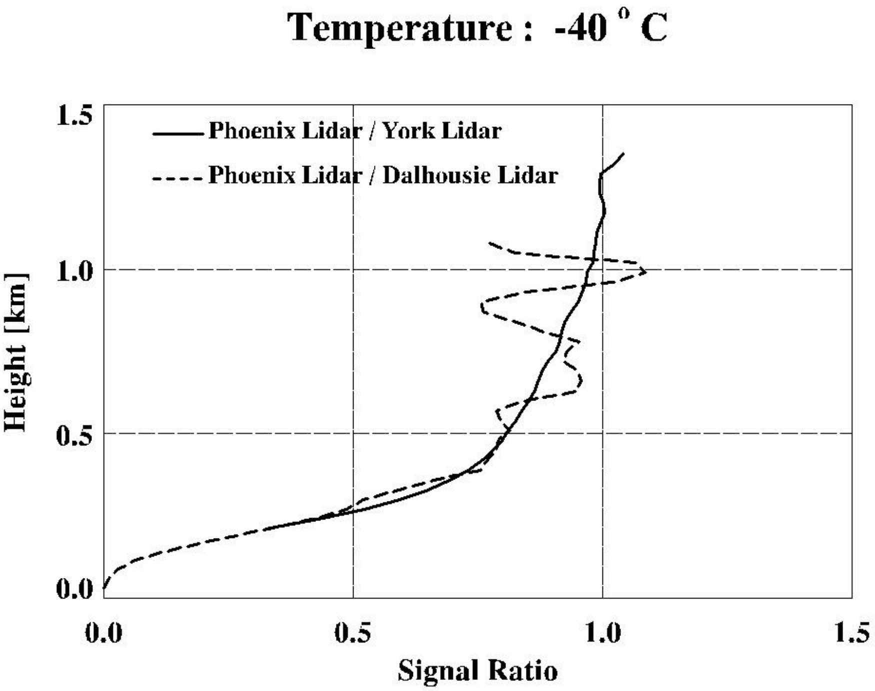

Temperature : -40 ° C

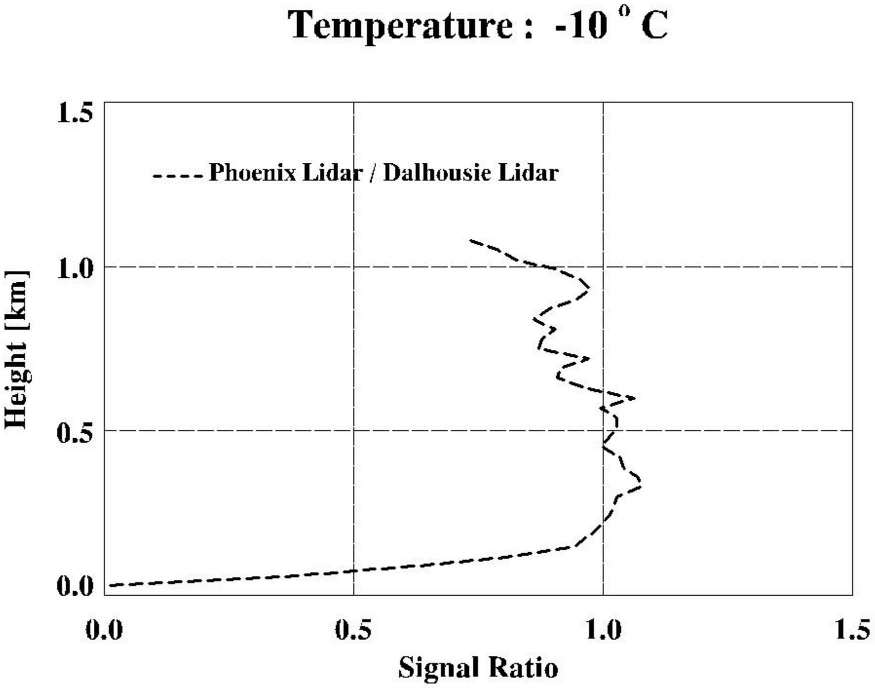

Temperature : -10 ° C

Figure 14. Ratio of the Phoenix lidar signal to the signals from the York and Dalhousie lidars at temperatures of -40° C and -10° C.

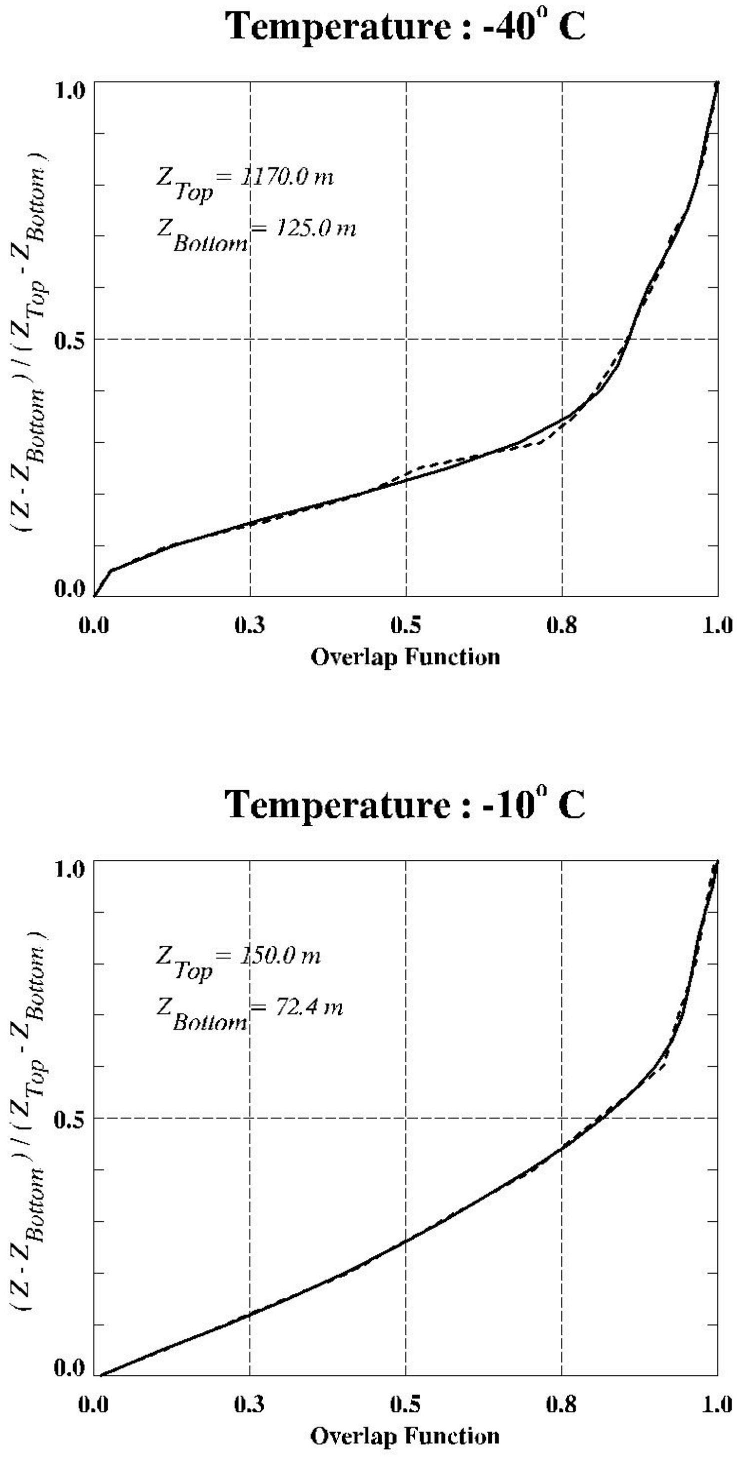

Figure 15. Overlap fraction as a function of normalized height for the temperatures of -40° C and -10° C.

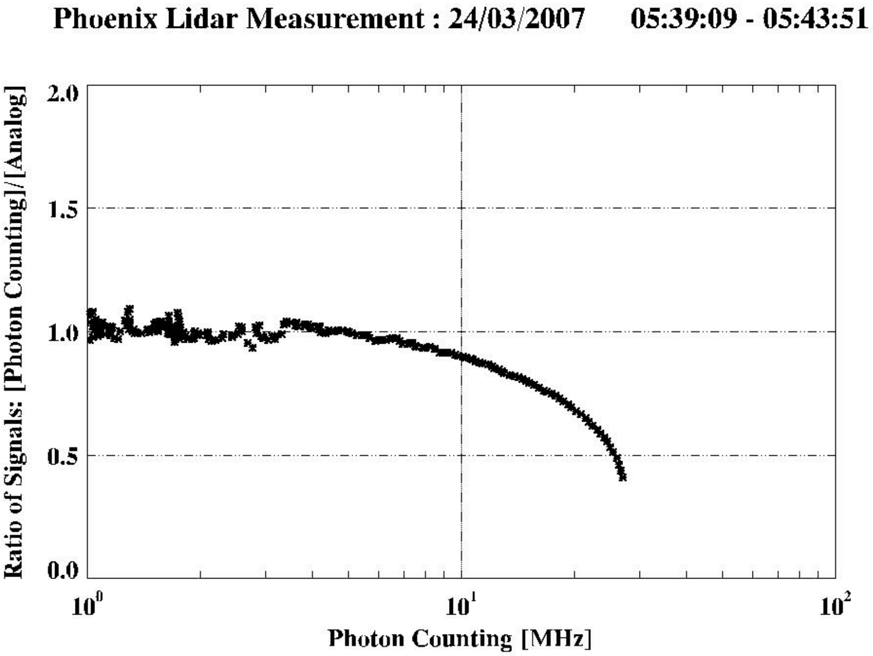

Figure 16. Ratio of Photon counting rate to analog signal as a function of the photon caouting rate. This has been normalized to a value of unity for count rates less than 5 MHz. The reduction from unity at count rates greater than 4 MHz is due to pulse overlap in electrical pulses prior to the discriminator.

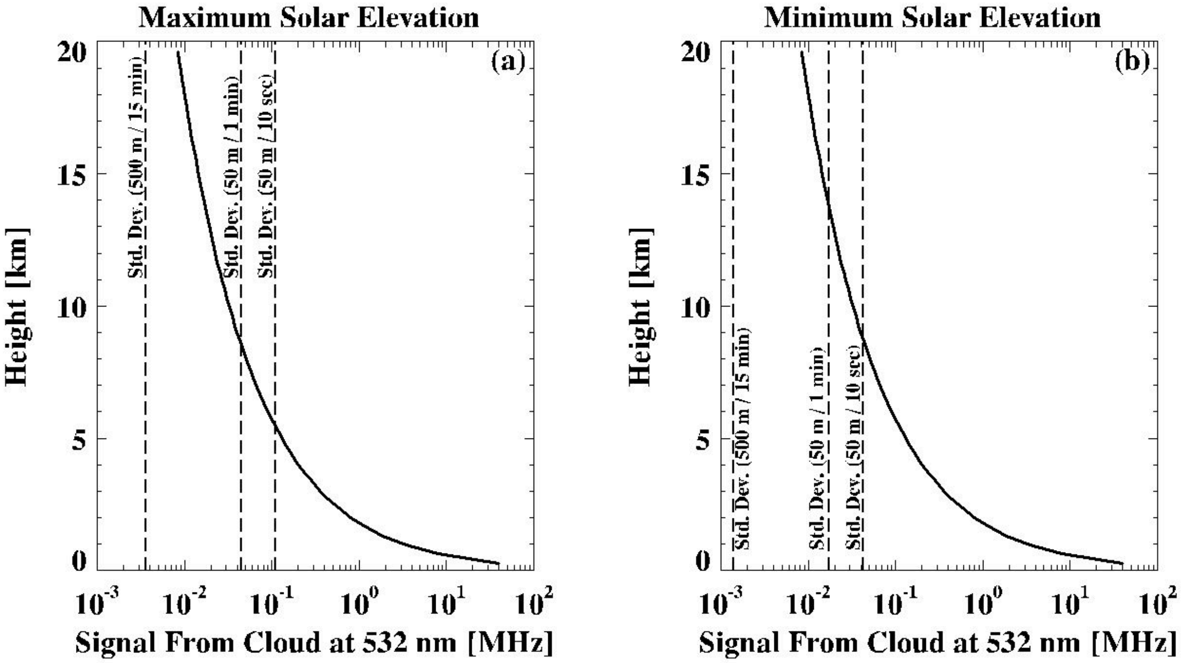

Figure 17. 532 nm photon counting backscatter signal from a cloud equivalent to the one in Fig. 10 (solid) compared with the standard deviation of the statistical fluctuation in the background skylight signal (dashed).

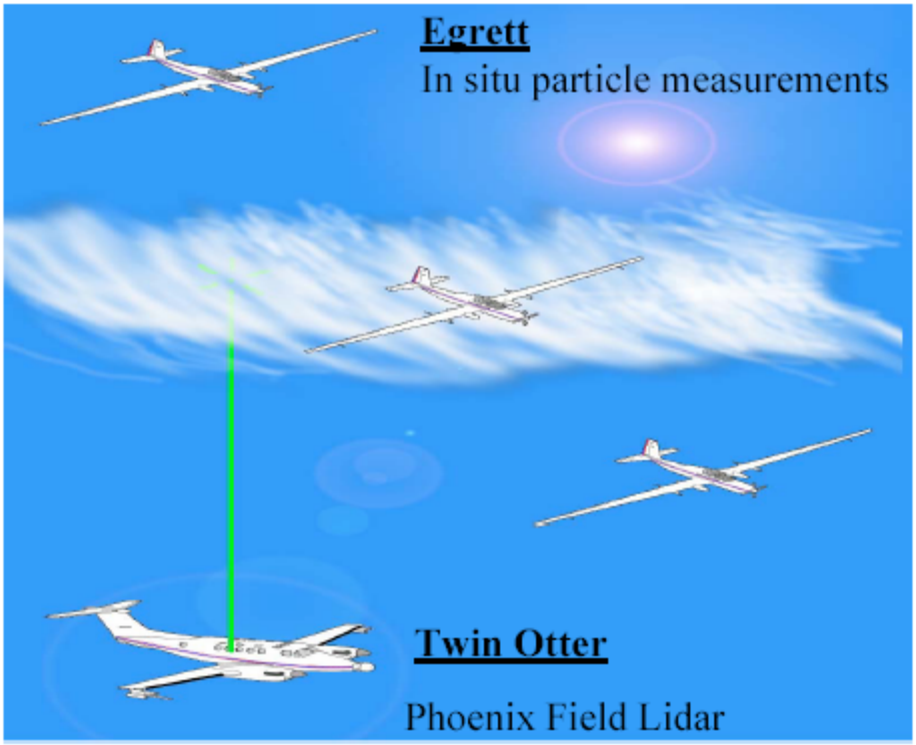

Figure 18. The arrangement of the aircraft in the cirrrus cloud measurement campaign.

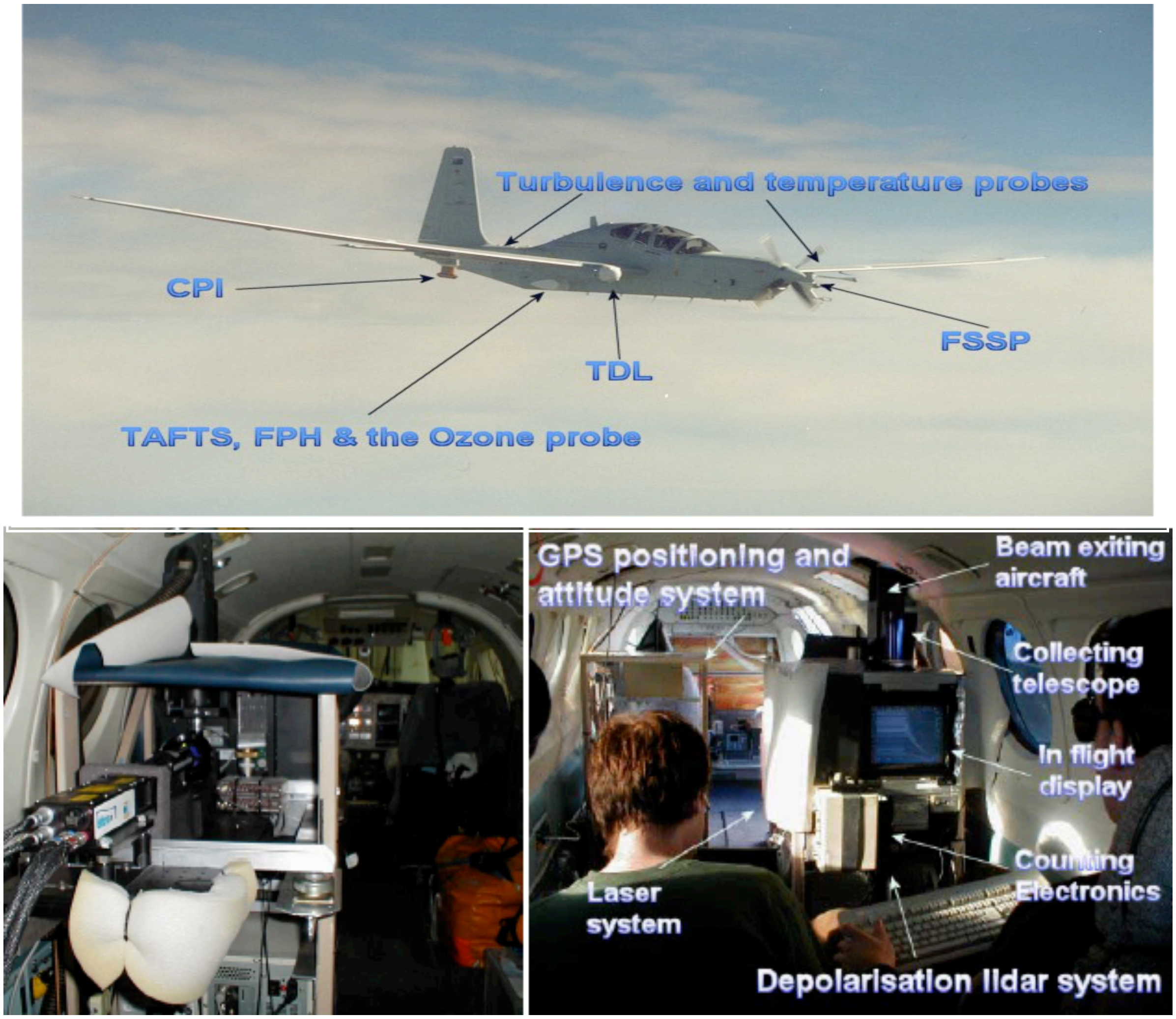

Figure 19. Images from the airborne cirrus cloud measurement campaigns. Top: a photo of the Egrett with the complement of instruments installed for the EMERALD campaigns. Bottom: photos inside the aircraft flying below the Egrett that carried a lidar that was equivalent to the Phoenix lidar.

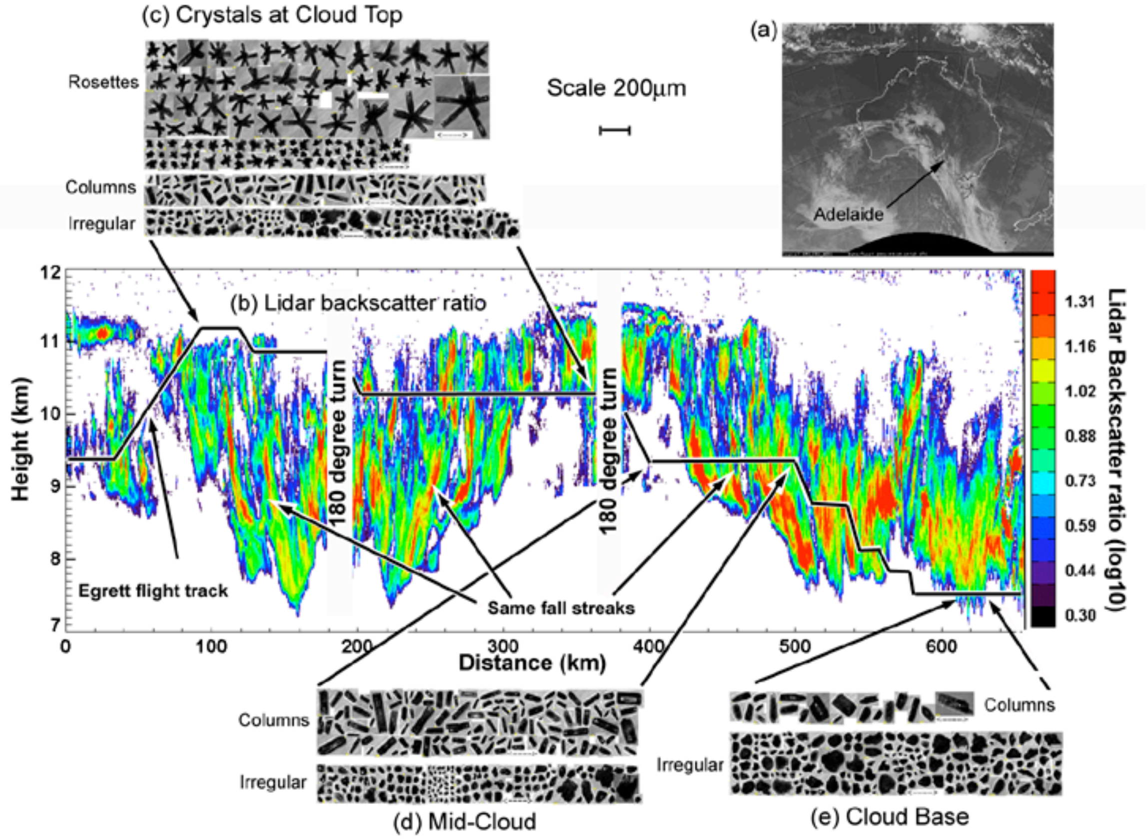

Figure 20. Airborne lidar and in situ measurements in a cirrus cloud. a) Satellite IR image showing the cirrus cloud system above southern Australia. (b) Lidar measurements from the King Air while flying directly below the Egrett. (c,d,e) Images of crystals recorded by the CPI on-board the Egrett. (From Whiteway et al., Geophys. Res. Lett., December 2004).

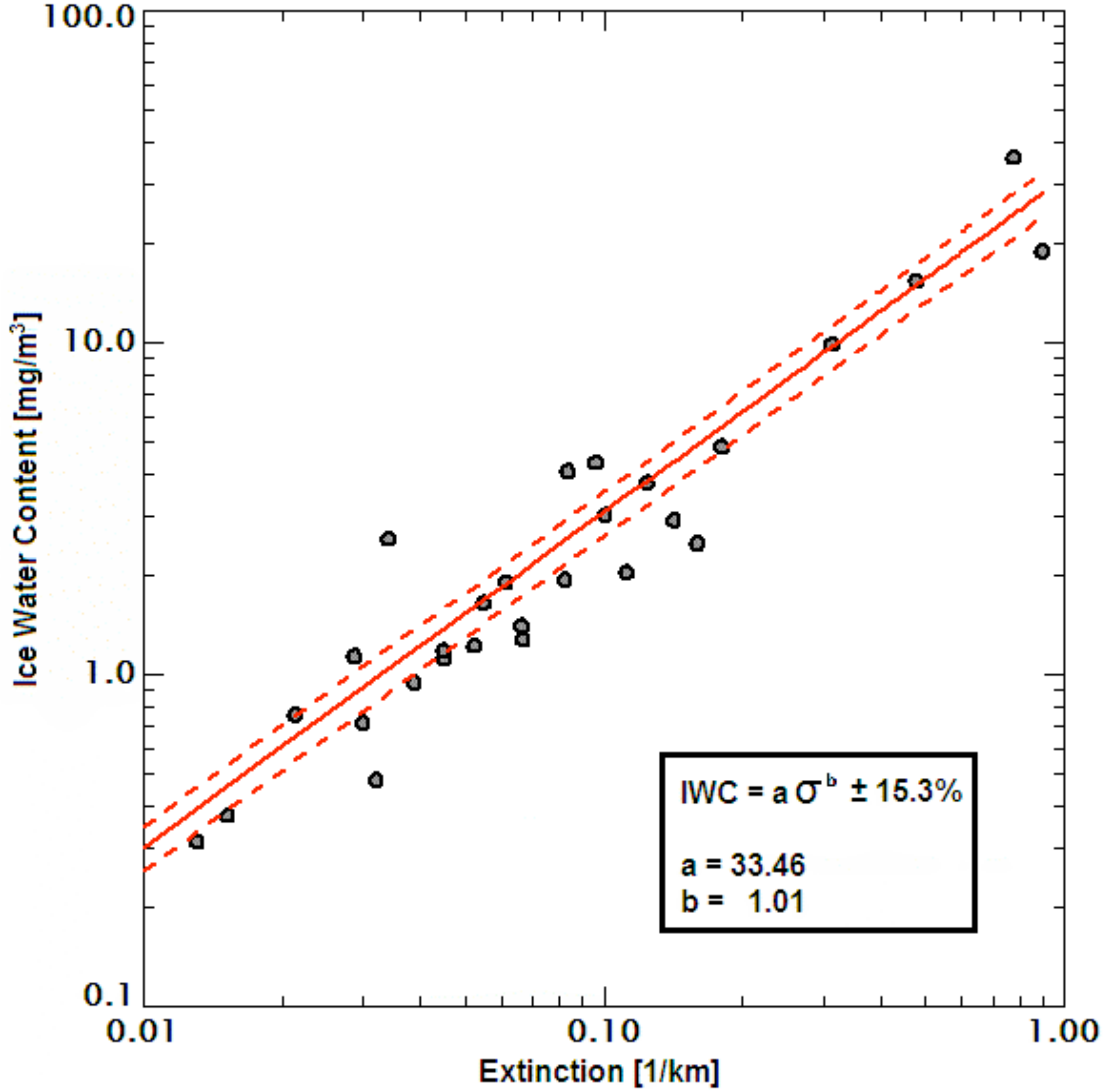

Figure 21. Scatter plot of extinction coefficient derived from lidar measurements and simultaneous in situ measurements of ice water content.

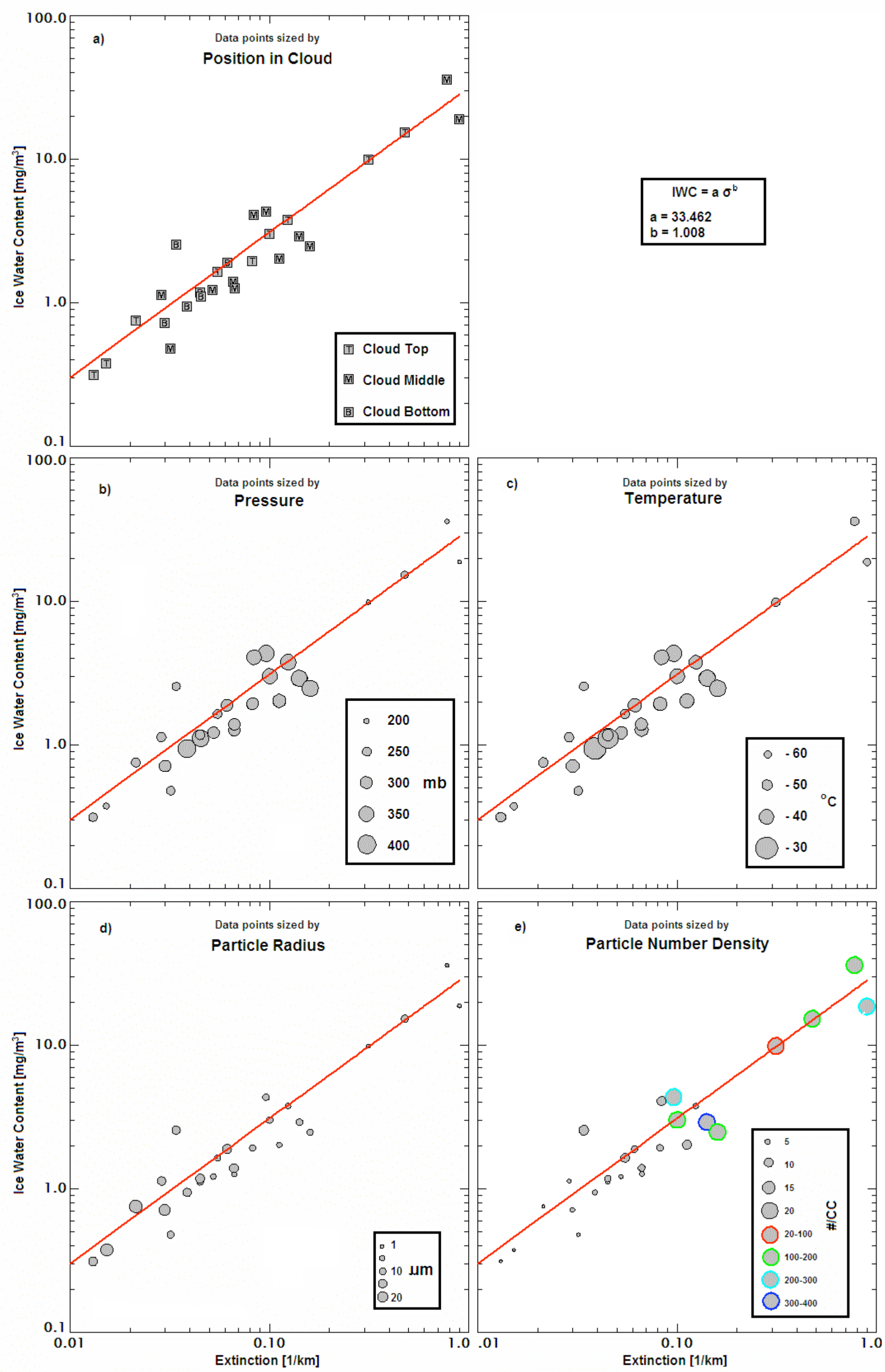

Figure 22. As in Fig. 21 with each data point marked according to (a) position in the cloud, (b) pressure, (c) temperature, (d) ice crystal radius, and (e) number density.

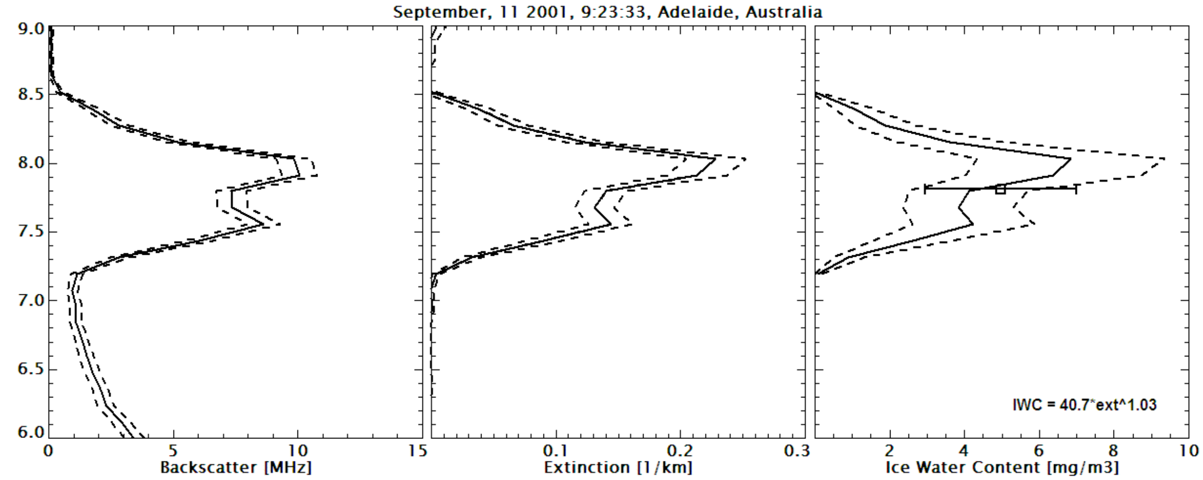

Figure 23. Lidar backscatter profile (left) and derived extinction coefficient (middle) and ice water content (IWC). The data point at 7.8 km is the in situ measured IWC. The dashed lines indicate the limits of uncertainty in the lidar measurement, and the error bar represents the standard deviation in the in situ IWC over the averaging interval of one minute.

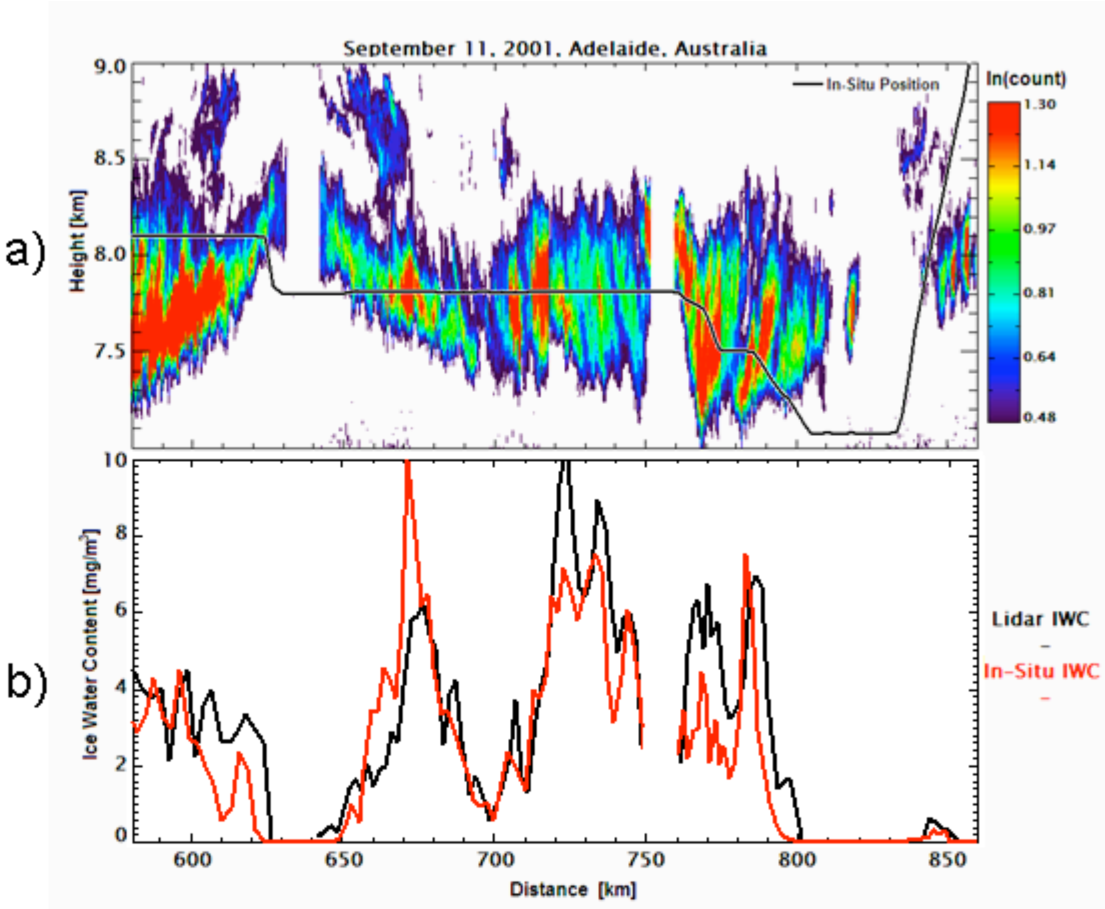

Figure 24. Measurements of a cirrus cloud from the Twin Otter lidar and Egrett in situ instruments on 11 September 2001. (a) Contour of the lidar backscatter signal with the black line indicating the position of the Egrett. (b) IWC derived from the lidar measurements at the position of the Egrett and also the IWC measured in situ from the Egrett.

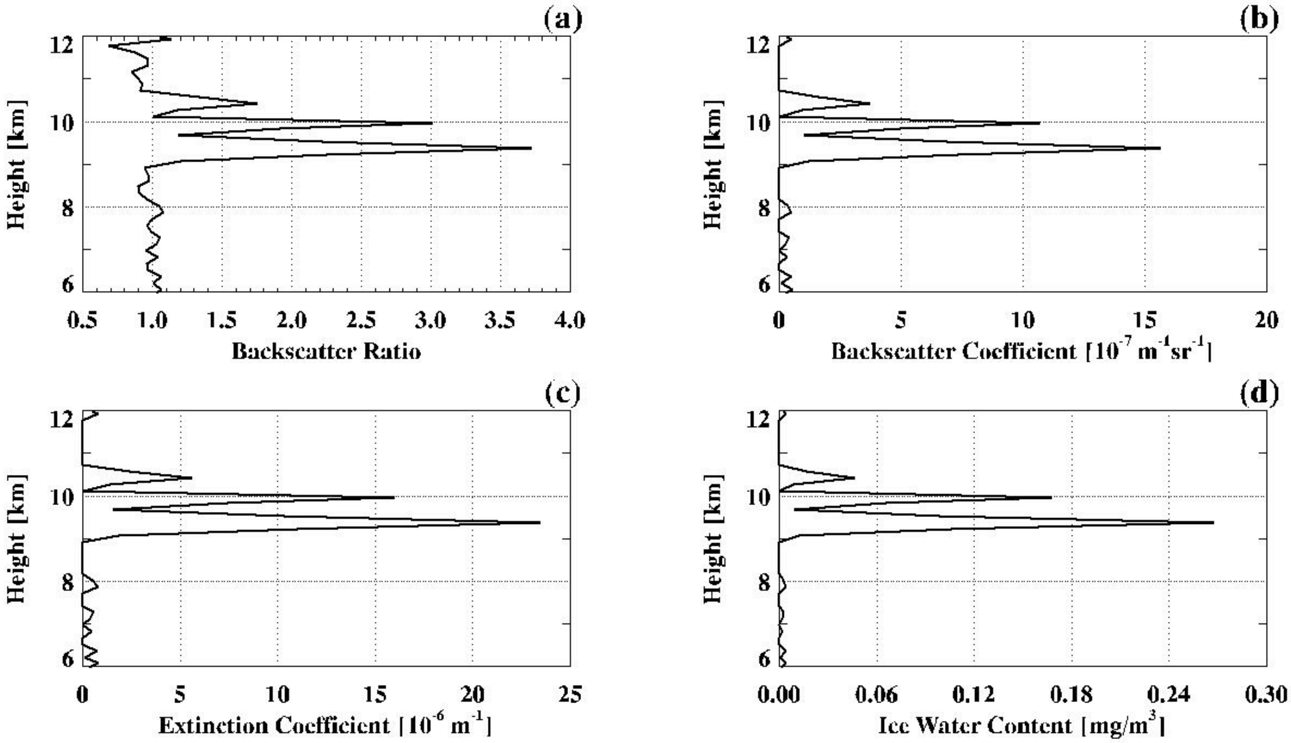

Figure 25. Four steps in the analysis of lidar data applied to the cloud backscatter signal in Fig. 10.